
Comparison of atmospheric simulations with paragliding flights

Léo Barrois

Abstract

Atmospheric models are not able to produce perfect forecasts even for idealized simulations over mountainous areas because of the spatial heterogeneities driven by the underlying topography. The scarcity and specificity of measurement campaigns remains a hurdle for the improvement of atmospheric boundary layer simulation over mountainous areas. Therefore, the main objective of this study are (i) to analyse the usefulness of paragliding and gliding flights in atmospheric studies, (ii) to compare parametrized and non-parametrized boundary layer convection models and (iii) to evaluate the benefit using a finer resolution in Meso-NH simulations applied over complex terrain. In this study, the Application of Research to Operations at Mesoscale (AROME) and Mesoscale Non-Hydrostatic Meso-NH atmospheric models are applied in the southern Alps. The evaluation and intercomparison of simulated results are conducted with the RADOME and Netatmo meteorological stations for potential temperature, water vapor mixing ratio, horizontal wind norm and with paragliding and gliding flights for the atmospheric boundary layer height and the vertical velocity field. The simulations evaluation shows that (i) Gliding and paragliding flights are unique and valid data to efficiently cover a large spatial and temporal extent within the ABL ; (ii) AROME show high skill for meteorological variables, whereas Meso-NH is a performing tool to simulate vertical velocities ; (iii) A higher resolution provides a better accuracy for a given atmospheric RCMs, though AROME 1.3 km proved better than Meso-NH 600 m and 200 m from meteorological variables. Overall, this study highlights the necessity to incorporate new data of atmospheric dynamics within the ABL, such as paragliding and gliding flights, to allow a full evaluation and tuning of RCMs, in particular over mountainous areas.

**Master Sciences de la Terre des Planètes et de l'Environnement****Attestation de non plagiat**

Je sous signé (Prénom NOM)

Barrois Léo

Auteur du mémoire (Titre)

Comparison of atmospheric simulations with paragliding flights

Déclare sur l'honneur que ce mémoire est le fruit d'un travail personnel et que je n'ai ni contrefait, ni falsifié, ni copié tout ou partie de l'œuvre d'autrui afin de la faire passer pour la mienne.

Toutes les sources d'information utilisées et les citations d'auteur ont été mentionnées conformément aux usages en vigueur.

Je suis conscient(e) que le fait de ne pas citer une source ou de ne pas la citer clairement et complètement est constitutif de plagiat, que le plagiat est considéré comme une faute grave au sein de l'Université, pouvant être sévèrement sanctionnée par la loi.

Fait à Grenoble,

Le 13/06/2023

Signature de l'étudiant(e)

Lu et approuvé, Léo Barrois

Contents

1	Introduction	4
2	Atmospheric circulation in mountainous region	4
2.1	The mountainous atmospheric boundary layer (ABL)	4
2.2	Paragliding	6
3	Method	7
3.1	Models	7
3.2	Datasets	9
3.3	Processing of flights - limitations	12
4	Results	17
4.1	Gliding and paragliding	17
4.2	Flights' comparison with models	19
4.3	Meteorological stations' comparison with models	22
5	Conclusion	26
Références		26
A	Annexes	32
A.1	Thermal elevation's distribution	32
A.2	Convection sampling	32
A.3	Surface variables for Meso-NH 600 and 200 m	34

1 Introduction

Tremendous progress in atmospheric modelling and weather forecasting occurred over the last decades thanks to improvements in physical parametrizations and numerical methods as well as an increase in computing power [Bauer et al., 2015]. Regional climate models (RCMs) such as Weather Research and Forecasting (WRF, USA) [Al-Yahyai et al., 2010], Consortium for Small Scale Modelling (COSMO, Germany) [Baldauf et al., 2011], the Unified Model (UM, U.K.) [Monteiro et al., 2022] and AROME (France) [France, 2008] are used to study short-term meteorological risks (storms, floods) but also to make climate investigations in multi-decadal simulations. Atmospheric models are not able to produce perfect forecasts because of the chaotic dynamic behaviour of the climate system [Lorenz, 1960]. Their application is particularly challenging over mountainous areas because of the spatial heterogeneities driven by the topography. Simulations based on idealised topography is a common framework to help the understanding of atmospheric variability over mountains [Wagner et al., 2014]. In these areas, there is a need for a better understanding of the variability of surface atmosphere exchanges, atmospheric boundary layer (ABL) and convection processes highly affected by mountains [Reitebuch et al., 2003, Bashmachnikov et al., 2013, Hierro et al., 2013]. This need does not concern only the improvement of weather forecast systems, but also the atmospheric components of GCMs that have to be improved to produce relevant future climate projections. [Wagner et al., 2014] highlights that a correct representation of the topography is essential to simulate a realistic mountainous ABL. Hence, a higher resolution, leading to a finer representation of the underlying topography, may enhance the prediction's accuracy [Zhou et al., 2014]. At finer resolutions, Large Eddy Simulation (LES) have been widely used to simulate the ABL dynamics over complex terrain [Vosper et al., 2013, Cuxart, 2015], and field measurement involving airborne measurements have been used to verify the models' predictions [Davies and Pichler, 1990, Bougeault et al., 1990]. Still, the measurement campaign restrain to a local diagnostics and would benefit from a larger extent. Meteorological stations do not cover sufficiently the complex topography of mountainous terrain to analyse mesoscale circulations or convection from surface data [Mandement and Caumont, 2020]. The present study proposes the use of paragliding and gliding flights to validate NWP models in the southern french Alps, being part of a wider effort to improve the representation of convection in atmospheric models at different resolutions.

The main goals of this study are (i) to analyse the usefulness of paragliding and gliding flights in atmospheric studies, (ii) to compare parametrized and non-parametrized boundary layer convection models and (iii) to evaluate the benefit using a finer resolution in Meso-NH simulations applied over complex terrain. To achieve these objectives, the atmospheric circulations within the mountainous ABL and paragliding activity are introduced in a first section 2. The models and processing of flights are then presented along their limitations 3. The results and simulation comparisons are discussed in the last section 4.

2 Atmospheric circulation in mountainous region

2.1 The mountainous atmospheric boundary layer (ABL)

The ABL, or Planetary Boundary Layer (PBL), is defined by [Stull, 1998] “as that part of the troposphere that is directly influenced by the presence of the earth’s surface, and responds to surface forcing with a timescale of about an hour or less.” The surface forcing includes terrain induced flow modification, friction and heat exchange. The strong horizontal and vertical heterogeneities of the surface enhance convective and turbulent motion during daytime in the ABL, impacting the exchanges of mass, energy and momentum between the

surface and free atmosphere. Therefore, the ABL has to be accurately simulated to describe surface-atmosphere exchanges in single columns models (SCM) that are finally applied spatially in GCMs [Arakawa, 2004].

The convective motion in the ABL covers a broad range of spatial and temporal scales : from 1-100 m, 10-600 s for the turbulence, 1 km for buoyant thermal organization, 1-5 km for cumulus clouds, 10-20 km for cumulonimbus clouds, 500-1000 km for cyclones up to the global atmospheric circulation with 1000-5000 km for the Hadley and Walker circulations [Rio and Hourdin, 2023]. Though the large amount of different convective scales, no clear gap between the scales in the energy spectrum has yet been observed, there is a continuous scaling from turbulence to large-scale convective motion.

Mountainous ABL circulations are impacted by the overlying complex topography. During daytime, specific mountainous atmospheric buoyant thermally forced motions are organised following the valleys (valley winds) and slopes (slope winds). This specific organisation enable gliders and paragliders to efficiently search for ascending vertical currents.

The diurnal valley winds are consequences of differential heating caused by topography [Cuxart et al., 2016], known as the "bulk effect", i.e. the same amount of radiative short wave downward (long wave upward) flux warms (cools) a more restrained volume of atmosphere inside deep valleys than in plains, hence creating a gradient of potential temperature between the plain and the valley atmosphere. A differential heating may be observed as well between the sides of a valley with different sun exposition, therefore leading to buoyant horizontal advection [Cuxart et al., 2016]. Valley wind fully develop until average $3-5 \text{ m.s}^{-1}$ wind speed and 500 metres depth. During nighttime, the circulation reverse : the surface long wave radiative cooling gradient, produce cold, dense air gravity induced valley to plain flow. Valley to plain nighttime wind have similar average speed and 300 - 400 metres depth [Rotach et al., 2015].

Slope winds are controlled by the warming/cooling of air parcels adjacent to the surface, hence are subject to strong turbulent effects. Slope winds are separated into two categories : anabatic and katabatic winds [Kirshbaum et al., 2018]. Anabatic winds are essentially controlled by the external forcing of short wave solar radiation and are associated with differential ground heating forced convection. Anabatic winds develop nearly instantaneously with the sunrise, vanish as quickly with late afternoon and are stronger under clear sky (stronger short wave radiative warming). They reach $1-5 \text{ m.s}^{-1}$ at 10-50 metres above ground level in the up slope direction within the temperature inversion zone, with a 20-200 metres depth [Rotach et al., 2015]. A subsiding down slope flow closes the mass balance on the upper up slope flow part of the ABL with comparable strength and depth. Anabatic wind mix and extend the ABL. The katabatic winds are more generally described as a consequence of surface long wave radiative cooling gradient, producing colder, denser air gravity induced down slope flow. They develop nearly instantaneously during the early evening as the surface begins to cool, vanish at sunrise and are stronger under clearer sky (stronger long wave radiative cooling). They reach $1-4 \text{ m.s}^{-1}$ at 1-15 metres above ground level in the down slope direction within the temperature inversion zone, with a 3-100 metres depth [Rotach et al., 2015]. An ascending up slope flow closes the mass balance in the ABL with comparable strength and depth. Katabatic winds stratify and constrain the ABL vertical extent. Because of the different inertia of valley winds and slope winds, the two circulations have similar daily cycle staggered in time.

Shallow convection may be defined as the atmospheric circulations impacted by surface fluxes that do not contain precipitation, extending until the thermal gradient inversion layer. Deep convection correspond then to atmospheric circulations disconnected to the surface fluxes, containing precipitations and extending over the thermal gradient inversion layer. In that sense, valley and slope winds are part of shallow convection. Indeed, [LeMone and Pennell, 1976] shows that cumulus clouds are the saturated part of buoyant thermal plumes.

Moreover, deep convection may be triggered by the elevation by orographic waves of capped moist air parcels [Hierro et al., 2013].

Several ground-based and airborne measurement campaign in the Pyrenees [Bougeault et al., 1990, Lothon et al., 2014] and in the Alps [Davies and Pichler, 1990, Bougeault et al., 2001, Laiti et al., 2014] providing fine-scale measurements of the weather condition during the past decades were confronted with LES over complex terrain [Rotach and Zardi, 2007]. Still, the measurement campaigns restrain to a local diagnostics and there is a clear lack of observational data to fully understand atmospheric processes over mountainous areas and validate atmospheric models. As processing free pollutant density vertical profile to image (un)stability in the ABL is quite accepted [Mahalakshmi et al., 2011], a paragliding addict researcher in the field of convective ABL would easily suggest the use paragliding trajectories as airborne measurements of the ABL properties.

2.2 Paragliding

A paragliding is an aircraft (a means of transport within the earth's atmosphere) derived from the parachute. It consists of a wing (or sail) from which the harness (driver's seat) is suspended by lines. The pilot is able to slightly deform the wing profile in order to take advantage of the vertical and horizontal winds to ascend and subside within the ABL. Gliding is flying with an unpowered aircraft, though a motor may be on board for takeoff and stall prevention.

The wing or canopy of a paragliding is an ram-air airfoil, able to generate significantly more lift than drag. It typically has an area of 20-35 square metres and a span of 8-12 metres for a weight of 3-7 kg. The wing is formed of two layers of non-porous fabric (light-weight nylon fabric such as ripstop nylon [Textile]) connected by internal material to form a row of cells [D.C. Jalbert]. These cells are partially supported by semi-flexible plastic rods to provide the profile of the wing extra stability. While the cells of the leading edge and wingtips are closed to form a cleaner aerodynamic profile, the internal cells are pierced by little holes to allow a free flow of air from the inflation opening, slightly backwards on the underside of the wing, providing the wing a shark nose shape [Pieri]. The shark nose shape slows down the wind close to the inflation opening, providing an air pressure of the air flow closer to the stagnation point pressure of the wing, enabling a good inflation of the wing. Such strong inflation properties result in a greater stall resistance at low speed and longer brake range. The lines are crafted from strong, light material (UHMW polyethylene or aramid, up to a breaking strength of 550 N for a 0.66 mm-diameter line [Uzochukwu]) organised in a tree structure from the pilot to the canopy. Recreational wings acknowledge a speed range from 6 to 15 $m.s^{-1}$, from the stall speed (wing folding, loss of the inflated profile) to maximum speed, relative to the air mass [Miller]. The combined mass of the wing, harness and instruments is around 12-22 kg. In comparison, gliders cover a usual speed range of 20 to 60 $m.s^{-1}$ for more than 200 kg.

Gliding and paragliding dynamics are highly similar as their source of motion relies on atmosphere dynamics. The two aircrafts are however very different. Unlike paragliding, gliding are made out of solid material, assembled into a structure with a much higher glide ratio (horizontal distance divided by the vertical distance over a given time, which can be seen as well as the Lift/Drag ratio, i.e. the lift intensity divide by the drag intensity felt by the aircraft), from 8:1 to 11:1 for a paraglider and from 17:1 to 70:1 for a glider [Wikipedia, a]. Hence, gliders may stay much longer time at high altitude, reach much higher speed (up to 300 $km.h^{-1}$), much higher altitude (23 000 metres above sea level [Jackie] (made possible by the ability of the glider to follow gravity wave above the ABL, where a paragliding would not be able to fly over strong winds faster than 15 $m.s^{-1}$) and are much lesser subjected to stall.

Paragliding and gliding may carry instruments, such as radios to communicate with other pilots, instructors, air traffic controllers. Variometer to account for a precise measure of ascending and subsiding rates (up to 1 cm.s^{-1}). GNSS, mainly during flying competitions to demonstrate that way-points have been correctly passed, but also to extract trajectories data in order to infer in situ atmospherics's properties. Increasingly, smartphones are used to replace GNSS. Moreover, during competitions, pilots are obliged to bear an emergency parachute and a helmet. Indeed, risk of lesion during practice concerns the whole body from scratch to severe trauma, sometimes causing the death of the pilot [[Soleil](#)].

Paragliding acknowledge numerous competitions, festivals (The biggest one being the Coupe Icare, at Saint-Hilaire du Touvet, Grésivaudan, France), specialities (distance, duration, maximum height, tumbling, thermalling, speed, dynamical, tandem) and is practiced worldwide. Paragliding and gliding are practiced mostly in mountainous areas where slopes and valley winds prompt strong vertical motion.

The ability of a pilot to fly resides not only on his.er ability to control its canopy or aircraft, but as well on his.er knowledge and experience of atmospheric boundary layer dynamics relative to mountainous or plain areas. As a given flight depends on the state of the atmospheric boundary layer, paragliding and gliding flights may be of great use to investigate the atmospheric boundary layer evolution through time. Moreover, paragliding and gliding flights offer the unique opportunity to extract information from ascending velocities, and specifically thermals (i.e. ascending vertical currents within the ABL) along their life cycle.

A quick review of the paragliding (gliding) history can be found in [[Criss](#)] or [[Wikipedia](#), [b,a](#)]. For a further reading on paragliding dynamics please refer to [[Landell-Mills, 2021](#)], [[Benedetti, 2012](#)].

3 Method

In the Alps, the heat wave from the 11th to the 25th of August was the hottest on record. In Grenoble, temperatures reached an absolute local record of 42.6°C on the 24th. The 0°C isotherm exceeded 5000 metres altitude, causing glaciers and permafrost to melt on the summits. These scorching days are particularly interesting for studying the thermal forcing of topography on atmospheric convection. In fact, during this period, shallow convection materialized by cumulus clouds only appeared over mountainous areas.

The absence of high-level clouds and synoptic forcing makes these days ideal for simulating the mountainous ABL's daily cycle. These meteorological conditions are also ideal for gliding and paragliding, enabling altitude record-breaking (each landings on the summit of Mont Blanc occurred during heat wave, nowadays forbidden). A large number of flights are hence registered, providing a wide range of data within a very thick boundary layer.

The present study will therefore be based on six consecutive days of this ideal period from the 19th to the 24th of August. The models used to simulate the atmosphere's characteristics (potential temperature, water vapor mixing ratio, wind components, ABL's height, vertical velocity field) are herein presented, followed by the observation dataset and their processing.

3.1 Models

Meso-NH and AROME are used to simulate the atmosphere because, as developed by Météo-France, the data are available for the period under consideration. This work is also part of N. Philippot's thesis, the aim of which

is to simulate fine-scale convection in mountainous regions using Meso-NH. This choice also makes it possible to compare a parametrized (AROME) and a non-parametrized (Meso-NH) boundary layer convection.

3.1.1 Meso-NH

The following section has been mostly documented by [Lac et al., 2018]. Meso-NH is a non-hydrostatic mesoscale research-oriented atmospheric model (Mesoscale Non-Hydrostatic) developed by the Laboratoire d'Aérologie (UMR 5560 UPS/CNRS) and by CNRM-GAME (UMR 3589 CNRS/RADOME) introduced in 1998 by [Lafore, 1997]. Based on non-hydrostatic equations accounting for Earth's sphericity, it may be applied to a broad range of scales, from synoptic (10^3 km , several days) to turbulent (1 mm to 1 km, 1 second to 1 hour) scales, for a large panel of applications in atmospheric physics and chemistry : aerosols, electricity and lightning, hydrology, wild land fires, volcanic eruptions, and cyclones, etc Meso-NH acknowledge grid-nesting and parallelized code technique (able to run on computers with more than 100 000 cores [Nagel, 2022]), enabling it to run on fine resolution in experiments that can serve as references to develop physical parametrizations of global climate models and numerical weather prediction models [Arakawa, 2004].

The set of Meso-NH's equations cover the Reynold's decomposition (i.e. decomposing the flow in a explicitly resolved large scale part and a parameterized sub grid scale motion) of conservation equations of momentum, humidity, mass and entropy [Lafore, 1997].

Meso-NH may be used as a Large Eddy Simulation (LES). During the numerical solving of the LES model's equations, the larger length scales are explicitly solved. The unresolved fluxes are parameterized. If not explicitly resolved, shallow and deep convection are parameterized with the eddy-diffusivity mass flux approach (PMMC09) [Pergaud et al., 2009]. This approach considers entrainment and detrainment rates of a buoyancy forced ascending air parcel starting from the ground. Entrainment and detrainment rates are defined differently whether inside (moist) or outside (dry) clouds. Eddy-diffusivity might be seen analogous to the effect of Brownian motion mixing transported quantities within a fluid. This parametrization scheme is still of good use reaching resolutions of 1 km - 500 m horizontal grid spacing as the grey zone of turbulence is reached. No deep convection scheme is necessary below 5 km resolution in convective situations [Honnert et al., 2016]. The sub-grid unresolved fluxes are parametrized with the turbulent kinetic energy (TKE) 1.5 order closure scheme. The local, sub-grid, turbulent flux is formulated negatively proportional to the vertical gradient of the transported quantity. The proportional constant depends on the TKE and the mixing length (a parameter defined by the distance an air parcel may travel up and down [Bougeault and Lacarrere, 1989], between the thermal stratification and the ground).

Mountainous ABL displays specific orographic induced circulations of the scale of the valleys and the slopes 2.1. A fine resolution is needed to explicitly resolve the larger energy containing scales (several hundred of metres) [Wagner et al., 2014, Rotach et al., 2015, Chow et al., 2019, Duine and De Wekker, 2020]. Indeed, [Cuxart, 2015] highlights that high resolution simulation of stably stratified nighttime valley cold pools [Vosper et al., 2013] should not be called LES, as the larger energy containing scales are of several decametres, smaller than the simulation resolution. High resolution LES have been widely used in complex terrain atmospheric simulation [Kalthoff et al., 1998, Medeiros and Fitzjarrald, 2015, Rohanizadegan et al., 2023].

The LES of this study has been performed with latest version 5.7 of Meso-NH with one-way nested grid effective resolution of 600 m and 200 m (father and son), forced by the numerical weather model AROME as lateral boundary conditions with time evolving fields in the southern Alps from the 19th to the 24th of August 2023.

3.1.2 AROME

The Application of Research to Operations at Mesoscale (AROME) is the non-hydrostatic RADOME's operational 1.3 km grid RCM since December 2008. It complements the global Action de Recherche Petite Echelle Grande Echelle (ARPEGE) [Courtier et al., 1994] and the limited-area model Aire Limitée Adaptation Dynamique Développement International (ALADIN) [Termonia et al., 2018]. Firstly designed to make short range forecasts, it has been built with the physical parametrizations of Meso-NH (micro-physics and sub-grid flux) and the adapted ALADIN's dynamical part. It is devoted to predictions covering 24-36 hours. The main advance of this weather prediction model is its fine resolution, explicitly solving deep convection, therefore strongly enhancing its skill for storm prediction [France, 2008], but also for extrem precipitation local events (i.e. cévenol events). AROME 1.3 km has been chosen to bypass the deep convection gray-zone (from 3 to 6 km) to avoid any sub-grid parametrization of deep convection processes. Such advance was made possible by the developments in supercomputers and observation systems. An important part of AROME is its data assimilation scheme. While mesoscale observations are assimilated following a 3D var assimilation scheme [Fischer et al., 2005], large scales dynamics are nudged to by ARPEGE's predictions.

AROME solve the nonhydrostatic fully compressible Euler Equations discretized [Wedi et al., 2009]. As the deep convection is solved at 1.3 km resolution, only the shallow convection is parameterized. The convection and turbulence schemes, shared with Meso-NH, are detailed in the previous section.

3.2 Datasets

The dataset used in this study is made out of paragliding and gliding trajectories and meteorological stations. The flight datasets are firstly presented, followed by a description of the meteorological networks.

3.2.1 Flights

Gliding and paragliding flights are retrieved from WeGlide (www.weglide.org) for gliders and XContest (<https://www.xcontest.org/world/en/>) for paragliders. WeGlide and XContest are online platforms enabling to visualise and score all the uploaded gliding and paragliding traces, enabling visualization (sometimes with sublime pictures). Scores are calculated based on the distance crossed, altitude, global shape by flights. Hence, the WeGlide and XContest dataset are biased by the will of pilots to register their flights online, so that everybody may have access to it. Far from all flights are represented. This shall not be an hurdle for the present study as the most valuable (in the WeGlide and XContest standard) traces are those that best represent the parameters further introduced throughout the study of traces (maximum height reached, maximum vertical speed sampled, section 3.3). However, a more complete covering, even for less trained pilots, might be beneficial, considering that even if not covering as much distance, some may reach cloud base or circle a thermal just fine. Moreover, pilots do not explore randomly the atmospheric boundary layer but fly over objectives (Ecrins mountain ridge or South-North round trips along the Alps for example). Similarly, certain terrains are impassable due to the weakness or absence of thermals (lakes, deep shady valleys, everywhere during nighttime). Moreover, as gliding flights are towed during takeoff from aerodromes (altitude near 0 metres above sea level) until being able to glide on their own, in opposition with paragliding flights which takeoff from higher altitudes (approximately 1500 m asl mean), the lower altitude ranges are mostly covered by glider's early flights and landings.

The incompleteness of this data is however counterbalanced by the good quality of the flights data. Each flight

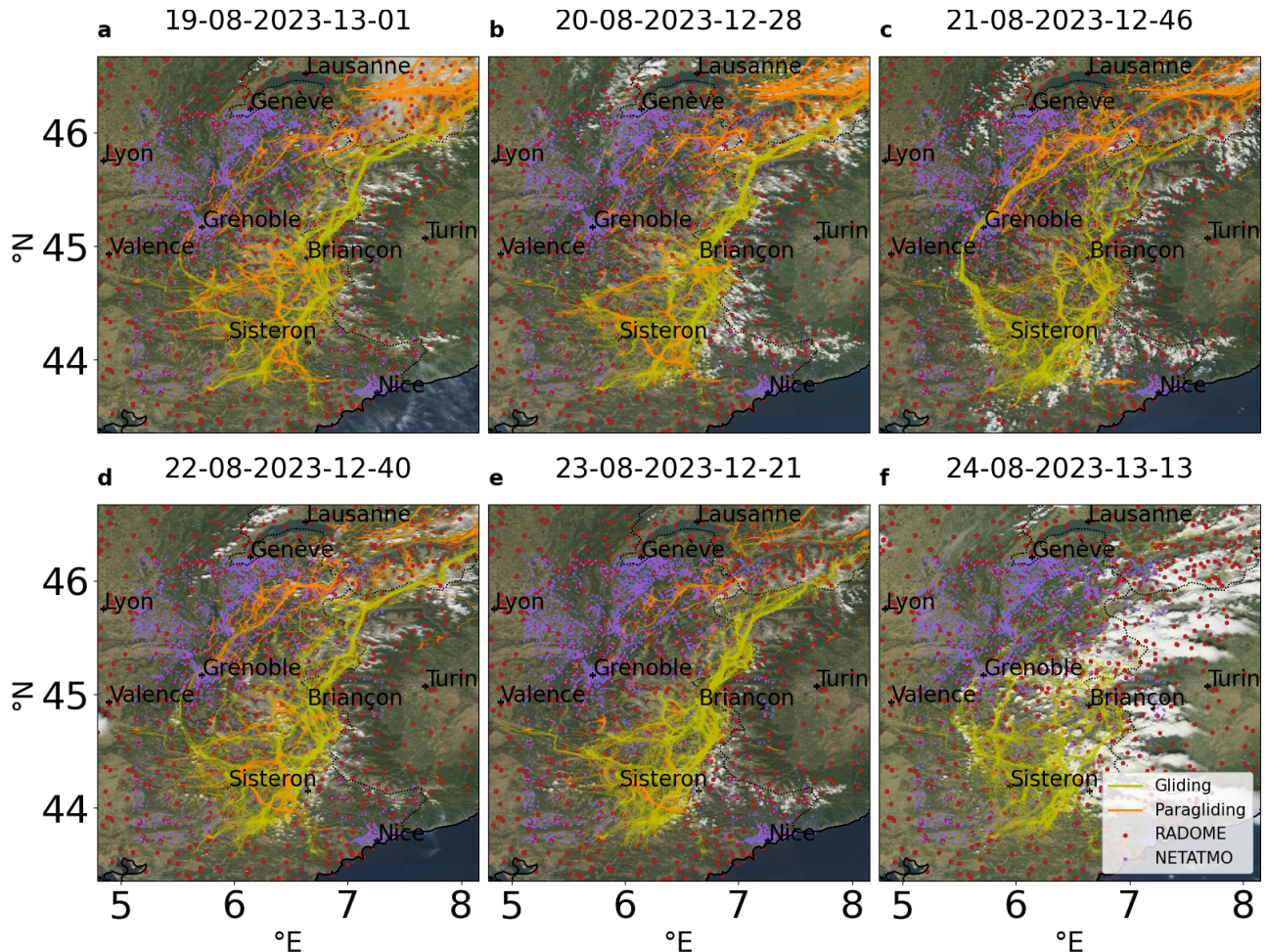


Figure 1 – Atmospheric daily datasets available for this study over south-east France: Netatmo stations (purple dots), RADOME stations (red dots) paragliding traces (orange lines), gliding traces (yellow lines) superposed to a MODIS satellite view (time of occurrence in the title) of the surface including cloud cover from the 19th to the 24th August 2023 (panels abcdef). Coastlines are solid black lines, borders dotted black lines.

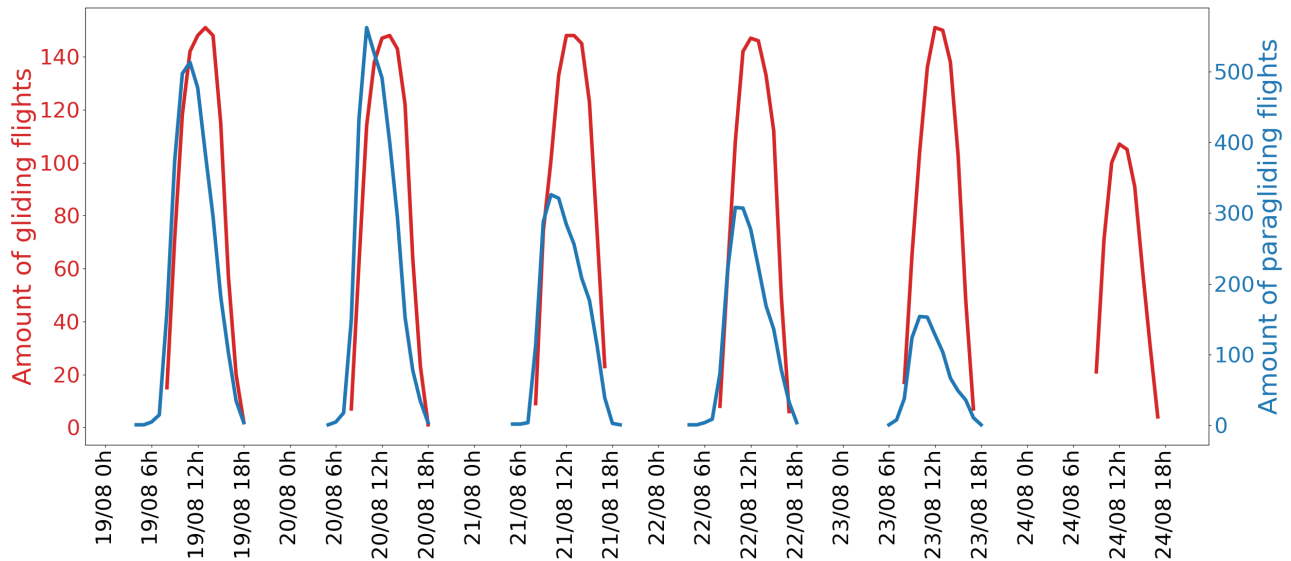


Figure 2 – Hourly number of flights from Sunday the 19th to Thursday the 24th of August 2023 for paragliding (blue, scale on the right side) and gliding (red, scale on the left side) flights. Please note that the range is higher for paragliding flights. The paragliding flights have not been download for Thursday the 24th.

is registered in the FIA (Federation International of Aeronautics) format : GNSS longitude, latitude (next to their accuracy) and time are listed every seconds. For gliding, traction or ignition of an engine is recorded. The name of the crew, the model of the aircraft, the fuel level, the flap position, motor temperature, the manufacturer of the pressure sensor, the time of the photos... are also listed. However, flights data do not list any record of the actions of pilots on their aircraft or canopy. Therefore, only specific situations are used to infer ABL characteristics in section 3.3).

The flights used cover the french Alps from Marseilles to Geneva, Lyon to Milan, from the 19th to the 24th august 2023 during daytime, figure 1. Firstly, in term of spatial distribution, the paragliding and gliding flights do not cover equally the same regions. As the gliding flights closely follow the main Alpine mountain ridge (abcde) from the regional natural park of Queyras until at least the natural park of Binn valley, with a remarkable spread around the Ecrins national natural park and along the eastern plateaus of the Vercors regional natural park. The strongly crossed sites on the southern part of the domain, below 44° latitude north and from 5.5° to 7° longitude east, are aerodromes where takeoff and landing for gliding flights (Saint Martin de Castillon, Puimoisson, Vinon...). The paragliding flights represent much more the Chartreuse, Bauges regional and Gruyère Pays d'Enhaut national natural parks hence highlighting different major pathways. One particularly crossed triangular pathway links Briançon, cross the southern part of the Ecrins national park to reach Sisteron, head back north west until the Baronnies Provençales regional natural park and head back to Briançon. In figure 1, the appearance of deep convection with high vertical velocities might explain the change of morphology of the passageway of the gliding traces. During the Thursday 24th, a much lower amount of gliding flights cover the highest part of the Alpine mountain range, though the Sisteron - Baronnies Provençales regional natural park - eastern Vercors regional natural park region is still much crossed. Secondly, as shown in figure 2, unlike it might seem on figure 1, much more paragliding than gliding flights are registered each day (more than 900 paragliding flights versus 158 gliding flights on the Sunday 19th of August) . However, the mechanical properties of gliders enable them to follow longer route with much higher speeds, therefore resulting in a larger spatial exploration for a lower amount of individual trace. Moreover, unlike gliding flights, paragliding flights contain some short flights, commonly called 'splash' ('plouf' in french), covering a much constrained spatial domain. Lastly, as previously discussed in section 2.1, the meteorological state of the Sunday 19th to the Thursday 24th of August is remarkable as the absence of synoptic forcing and large scale cloud cover highlight the impact of orography on the cloud formation. The panels (a) to (e) from figure 1 offer a qualitative view of the formation of the clouds on the local maximum of the Alpine mountain range. On the panel (f), the satellite snapshot makes visible the occurrence of deep convection transported by high altitude synoptic wind. Indeed, a heatwave alert was released on the 22th, with temperature reaching a maximum of 42.6 °C in Grenoble, soon followed by a storm alert.

A near constant number of gliding flights are registered everyday (154 to 158), a much larger amount of paragliding flights, though strongly decreasing because of storm prediction for the last days (404 to 941). The temporal availability of paragliding and gliding flights is displayed on figure 2. With the end of the week end, the Monday 21st of August shows a strong decrease of paragliding flights (from 600 the Sunday 20th to 300 the Monday 21st), whereas the amount of gliding' flights remain constant until the Wednesday 23th. This difference might be explained by the finite number of gliders available at aerodromes (158 from the 19th to the 24th) and the large amount of canopy (each paragliding operator owning one), considering that at least 158 glider pilots were not working from the 19th to the 23th, and that at least half the paragliding pilots were working during Monday 21st week. The strong decrease, first of the amount of paragliding flights the 23th, then of the amount glider flights the 24th, may be caused by the vicinity of storm that occurred later in the region, the paraglide

canopy being quite more sensible to turbulence than rigid glide [Benedetti, 2012].

3.2.2 Meteorological stations - RADOME and Netatmo

The RADOME network (Réseau d'acquisition de données et d'observations météorologiques étendues) [Tardieu and Leroy, 2003] is an automatic network of more than 550 stations, including RADOME network, providing field measurements for pressure, temperature, water vapor mixing ratio, precipitation, wind norm and direction. These data are expected to match high quality standards. RADOME stations cover the whole domain homogeneously in the horizontal plain, from sea level to more than 3000 elevation metres Fig. 1.

Netatmo stations, developed in 2012, are the first product from a french enterprise specialised in connected devices. These domestic meteorological stations capture temperature, water vapor mixing ratio and pressure. Initially not designed to assess scientific questions, they were first used to better constrain small-scale meteorological variations previously invisible with the RADOME network alone in the case study of deep convection [Mandement and Caumont, 2020]. Net stations cover the whole domain with considerable inhomogeneity Fig. 1. A strong density of stations is found nearby cities (Grenoble, Chambéry, Nice), whereas more rural areas are scarcely covered by the Net network. Still, the average distance between two Net stations is far lesser than between two RADOME stations, enabling the Net network to capture smaller-scale meteorological variations than the RADOME network. However, these data are expected to match lesser good quality standards than the RADOME network, hence data processing algorithm was built in [Mandement and Caumont, 2020] to control the data quality in pressure, temperature and humidity. Still, further analysis will be conducted separately for both network.

The water vapor mixing ratio, temperature and wind data are retrieved at two and ten metres above ground level. Station's data are compared with the simulation's data interpolated on the 2D position of the station's with the cubic spline function from the numpy python package.

3.3 Processing of flights - limitations

After removing absurd GNSS motion (instantaneous crash or $0^{\circ}\text{N}, 0^{\circ}\text{E}$ teleportation), turbulent motion is filtered from flights with a 30 seconds Hann filter (the signal's Fourier transform is convoluted with the Hanning window in the spectral domain to strongly attenuate the high frequencies associated with turbulent motion). Then, the glider's early flight are removed as gliders are generally tracked by a plain or a onboard motor for takeoff.

As merely discussed in the previous section 3.2.1, paragliding and gliding trajectories can not be studied as exact tracers displaced only by atmospheric motion and gravity. However, pilots often follow objectives, such as reaching the highest altitude reachable, the ABL's highest or capturing the paroxysm of an ascending vertical atmospheric current, a thermal. These two paragliding and gliding targets are keys to infer the ABL characteristics from flights.

3.3.1 Atmospheric boundary layer height

Firstly, the highest altitude objective is investigated. Considering a sufficient amount of time in a given location, the assumption may be made that at least one pilot has reached the maximum height reachable during this period. Taking an amount of time sufficiently brief so that the ABL's height is unchanged (less than an hour [Stull, 1998]), the maximum height reached by the community of the pilots during that lapse time shall be comparable

with the simulated ABL's height during the period. The ABL's height estimate should depend on the exact same time when the highest point was reached within the spatial domain during the lapse time. If the highest point is reached in the early moments (resp. the last moments) of the time lapse, one may assume that the trajectories' estimation of the ABL's height shall be compared with the previous (next) simulation's estimation of the ABL's height (the simulations being saved hourly). However, in a first assumption for this study, the comparison will always be made between the trajectories and the next simulation's plain hour estimation.

The domain is sampled in a regular grid. The dependency of the measured maximum height reached by the paragliding and gliding flights with the surface of each grid box is shown on figure 3. For a coarser mesh ($n < 5$, grid box surface $> 70 \times 70 \text{ km}^2$), most of the information is lost and the maximum height reached is represented by few nearly global maximum alone. Whereas for finer mesh ($n > 120$, grid box surface $< 2.5 \times 2.5 \text{ km}^2$), it is not clear that sufficient amount of time has been passed within each grid cell to assure that the maximum height reachable has been effectively reached by paragliders and gliders, hence representing more the distribution of altitudes of a mean flight than the ABL's height. Therefore the ABL's physical properties are to be accounted for to choose a grid sampling in between the two extreme values $n < 5$ and $n > 120$. Considering a horizontal characteristic distance of variation around 10 km [Stull, 1998] for the ABL, a value of $n = 50$ has been chosen to sample the maximum height reached by the paragliding and gliding flights. This value of $n = 50$ shows a deviation from the asymptotic median value close to 0.25, meaning that this $n = 50$ mesh at least does not only represent the distribution of altitudes of a mean flight.

Following [Stull, 1998], the variations absolutely superior to 1 vertical kilometre per 10 horizontal kilometres within the maximum height reached by the flights is filtered. These high absolute horizontal variations in the maximum height reached may be the consequence of a box inside the mesh crossed by only the latest moment or a struggling phase of a flight, which contains no useful information concerning the ABL's height. Therefore, the grid box concerned by such rapid transition will be erased from the data.

3.3.2 Thermals

Secondly, the maximum vertical motion target is investigated. When meeting an ascending vertical current located in space, willing to take full advantage from the uplift, the pilot may intend to reduce to minimum her/his falling speed relatively to the air mass while circling close to the maximum vertical velocities of the ascending current. Knowing the minimum falling speed of gliding aircraft and paragliding canopy in motionless air (respectively -0.6 and -1.1 m.s^{-1} , determined quite accurately by the physics of the canopy and wing [Benedetti, 2012]), detecting the circling inside trajectories leads to a lower value for the thermal maximum speed for each circular trajectory. Then, as the circling is centered on the thermal's core, the horizontal motion of the pilot is a consequence of the horizontal motion (i.e. the horizontal wind) of the ascending current alone. Thermal's core motion is then approximated directly to that of the horizontal wind. Hence, detecting circular trajectories within flights leads to every wind components at a given position and time within the ABL. Moreover, detecting circular trajectories is a powerful and quite unique observation of the thermals' life cycle and vertical profile, as the pilots tend to follow thermals for tens of minutes, uplifting them self up to vertical kilometres. The vertical domain described by the circling episodes is however restricted. Pilots are more likely to fly from 1500 to 3500 metres above sea level (asl) while no circular trajectory is observed below 500 metres asl. What is more, reaching the upper part of a thermal, the vertical velocity tends to decrease, and the pilots to leave the ascending current. Another reason to leave the thermal early is to avoid cloud suck when the thermal is topped by a big cumulus. No clear diagnosis has been found to separate a trajectory that willingly leaves the thermal, and a trajectory that follows the thermal until it vanishes in the upper ABL or enters the cumulus.

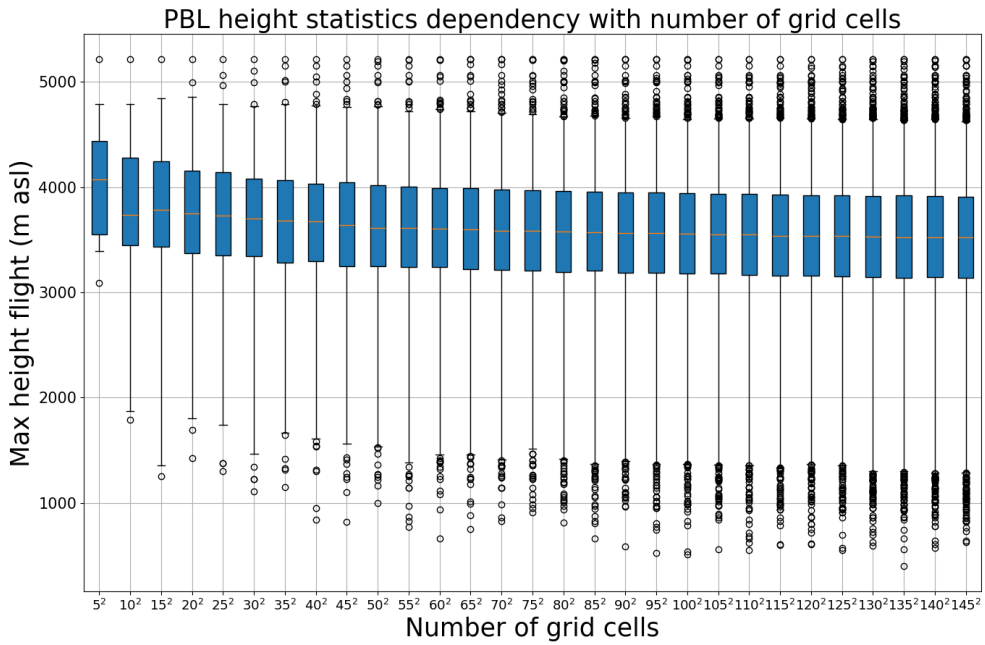


Figure 3 – Grid resolution’s influence on the sampling of the highest points reached by paragliders and gliders trajectories, over a domain containing n^2 grid boxes. For values of n varying from 5 to 145, the distribution of the maximum height reached within each boxes is represented by mustache boxes (the whiskers thin lines are the 90th and the 10th quantiles, the blue boxes the 75th and 25th quantiles, the orange bar is the 50th quantile, and the dots the extreme data points. The process is applied on the flights from 11 a.m. to 12 a.m. of Sunday the 19th of August.

The method used to detect the circular trajectories within paragliding and gliding flights is displayed on figure 4. As Fig. 4(c) shows a regular, localised roll of a thermal, Fig. 4(a) demonstrate a rather irregular, uncertain roll. This difference is observable within Fig. 4(b), showing the associated turning speed through time. The turning speed Fig. 4(d) from Fig. 4(c) shows two well separated thermalling ascents, with mean turning speeds of 12 .s^{-1} and turning speed oscillations (which might be a consequence of a not centered roll up : the pilot diminishing the radius of his/her trajectory when falling into a lower ascending velocity zone) amplitude of 2 .s^{-1} . The turning speed Fig. 4(b) from Fig. 4(a) shows a thermalling ascent cut with gliding periods and short circular trajectories, with a higher mean turning speed that Fig. 4(d) of 12 .s^{-1} and stronger oscillations of 4 .s^{-1} , leading to a crossing of the turning speed threshold. The differences between theses two thermalling ascents dwell in the difference between the two thermals and the different technical features of paragliding canopy and gliders, but also in the ability of the pilot to roll up a thermal. Therefore, all traces, event at the same position at the the same time, shall not contain the same amount of useful information.

The minimum turning speed threshold’s influence on the detection of circular trajectories is represented in figure 5. It is remarkable that paragliding flights may assume much higher turning speeds than gliding flights, described formally in [Benedetti, 2012]. Moreover, gliding flights contain generally more thermalling ascents than the paragliding flights, as glider’s flight are usually much longer, over longer distances. For lower minimum turning speed thresholds ($\dot{\alpha}_{thresh} < 3 \text{ .s}^{-1}$), slightly curved gliding trajectories are considered part of thermalling ascents. Whereas for higher minimum turning speed thresholds ($\dot{\alpha}_{thresh} > 16 \text{ .s}^{-1}$), very few pieces of trajectories keep above $\dot{\alpha}_{thresh}$ for at least 60 seconds to be considered as thermalling ascent. Hence, as a low $\dot{\alpha}_{thresh}$ leads to a large amount of poor quality thermal data, a too high $\dot{\alpha}_{thresh}$ leads to a poor amount of

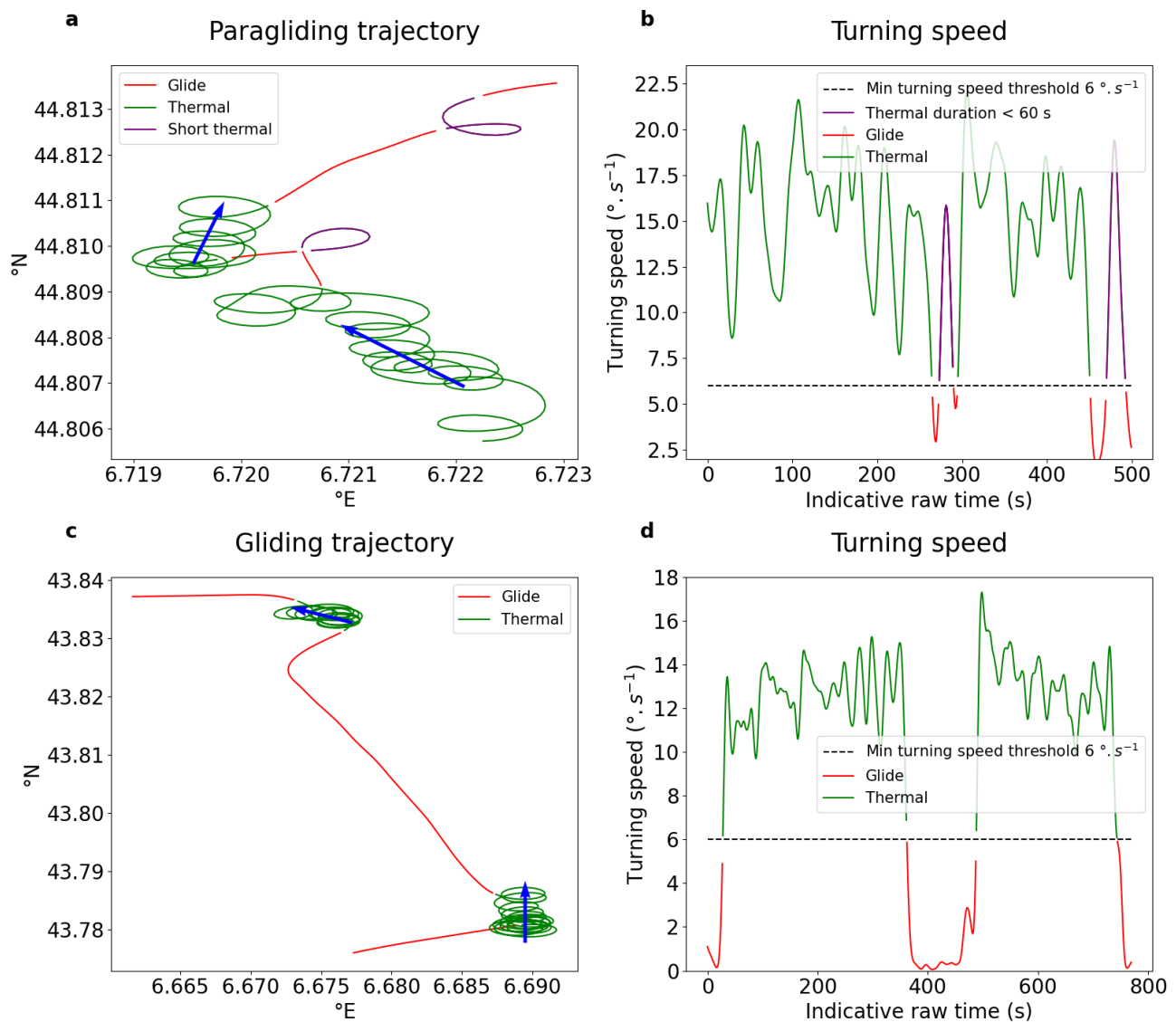


Figure 4 – Latitude-longitude trajectories of (a) paraglider and (c) glider and their corresponding turning speeds (bd). A thermal ascent is defined as a circular trajectory with a turning speed higher than $6^{\circ}.s^{-1}$ lasting at least 60 seconds with a positive vertical speed (green curves). Trajectories with lower turning speeds (red curves) or turning speed higher $6^{\circ}.s^{-1}$ during less than 60 seconds (purple curve) are considered as flight periods corresponding to other flight displacement. Indicative circling drift speed in blue arrows.

good quality thermal data. Without any physical argument to add, a $\dot{\alpha}_{thresh}$ has been arbitrary chosen at the intersection of the two major trends of the gliding median flight number of thermalling ascents, at $6^{\circ}.s^{-1}$, which is equivalent to 1 minute for a complete circle. An improvement would be to consider two different turning speed thresholds for gliders and paragliders, the paragliders' threshold being much higher than the glider's one.

3.3.3 Limitations

An inaccuracy of the comparison between simulation and flights lies within the definition of the ABL's height in the simulation : at the bottom of the clouds, or at the thermal gradient's inversion if cloudless. Even if it is not common (though forbidden for aviation issues) for gliding and paragliding flights to enter clouds (in which case the simulation and the flights describe the same quantity : the ABL's height), gliding and paragliding trajectories might pass through the edge of clouds, taking advantage of updrafts inside the clouds (hence describing another

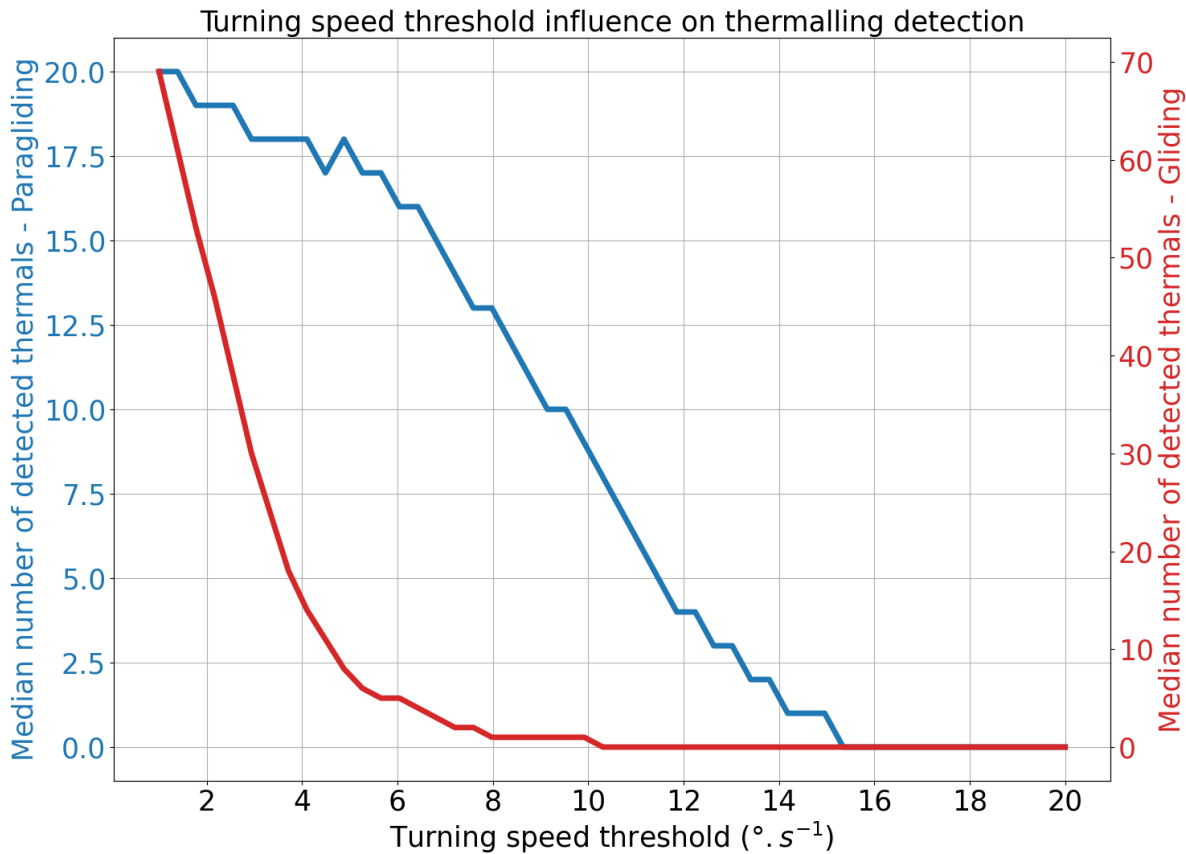


Figure 5 – Median of the number of thermalling episode detected with following the Fig.4's method as a function of turning speed threshold for paragliding flights (blue, vertical scale on the left side) and gliders (red, vertical scale on the right side) over the hundred longer flights of the 19th August.

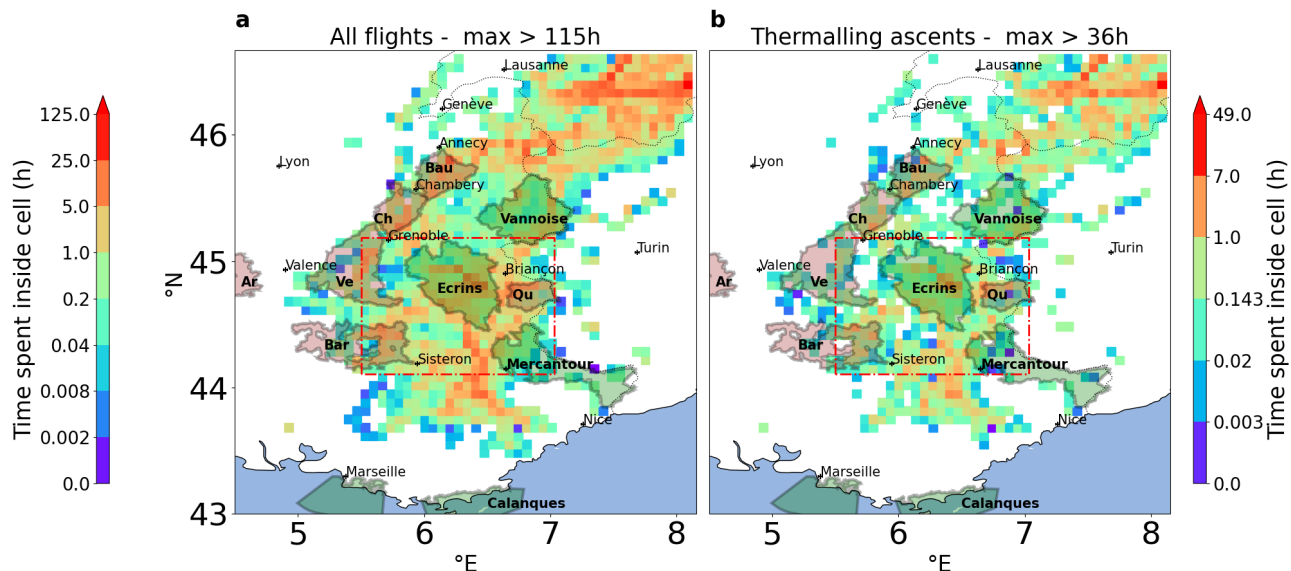


Figure 6 – Time coverage by pilots (hours per day, described with a logarithmic scale) the 19th August (first takeoff around 6 a.m., last landing around 8 p.m.) for (a) all traces including (b) thermalling ascent (defined with the 4's method), computed over a 10km resolution regular grid. National (green shading) and regional (brown shading) natural parks. The simulation domain is the red square area.

quantity than the simulation). This limitation of the use of paragliding flights to constrain simulation is even stronger considering the imprecise location of clouds within the simulation.

The validity of the ABL estimates from glider/paraglider data is function of the cumulative amount of flight time available over any domain during the lapse time considered, and the ability of pilots to better realise the objectives described in the previous paragraph (reaching ABL's top and capturing the highest vertical speed of thermals). As there is a lack of criteria to better describe the usefulness of a trajectory, the legitimacy of domain mesh is displayed on figure 6 through the amount of time cumulatively spent by the community of the pilots inside each grid cell during the 19th August, giving to each flight the same importance. From (a), it is remarkable that the mountainous areas are heavily crossed by the flights (the Alps are covered by a minimum of 2 to more than 115 hours per day per grid cell), the plain is neglected by flights (the plain accumulate lesser than 0.25 hours per day per grid cell, most of it not even crossed by any trajectories). From (b), one may note that as in (a), the circular trajectories are located over mountainous terrain, neglecting the flat areas. This shall be linked to the location of thermals over complex terrain, which in the absence of synoptic forcing during a sunny day, tend to form over local crests. The validity of the two assumptions described in the previous paragraph (the willingness of the pilots to reach the top of the ABL and capturing the highest vertical speed of thermals) shall then be valid only in the most crossed grid cells, within the mountainous terrain. Paragliding and gliding trajectories are therefore valid to address specific scientific questions relative to atmospheric boundary layer characteristics over complex terrain during daytime with flyable conditions. The sufficiently crossed spatial domains will then be referred as *legitimate* domains. The domain of comparison (red square 6) contains much heavily crossed grid boxes over complex and plain terrain, hence is *legitimate*.

4 Results

After presenting the inferred information from the gliding and paragliding flights, their comparison are followed by the meteorological station's network comparison with the simulations.

As for the comparison with simulations, regardless of the variable considered, the simulated distribution is the ensemble of simulated values located where observed values exist. Therefore, the simulated distribution contains as many point as meteorological stations (section 4.3) or grid boxes crossed by flights (section 4.1).

4.1 Gliding and paragliding

The flights are processed with section 3.3's method to infer the distribution of ABL's heights and the distribution of thermals speeds within the southern Alps between the 19th and the 24th of August 2023. The distribution and temporal variations of ABL's height will be first tackled (Fig.7 and 8), followed by a description of the ABL's daily cycle (Fig.9). Lastly, the distribution of thermals will be investigated (Fig.10). All along, flights data will be referred as observed data.

From 10 a.m. to 4 p.m. Fig.7(abcdef), the flights' spatial covering and mean maximum elevation increase. Then followed by a strong decrease from 5 p.m. Fig.7(gh) until nighttime. hence, the spatial covering and maximal elevation follow the evolution of the solar radiance's daily cycle (section 2.1). At any lapse time, thought more pronounced from 12-13h Fig.7(c) to 16-17h Fig.7(g), the maximum height reached by flights is quiet homogeneous within the central Alpine ridge. A strong decrease in the maximum height reached by flights is observed in lower altitude areas, which adapts to the current understanding of the ABL's height [Wagner et al., 2014]. However, this contour zone is not as *legitimate* as the central zone (section 3.3). Moreover, as

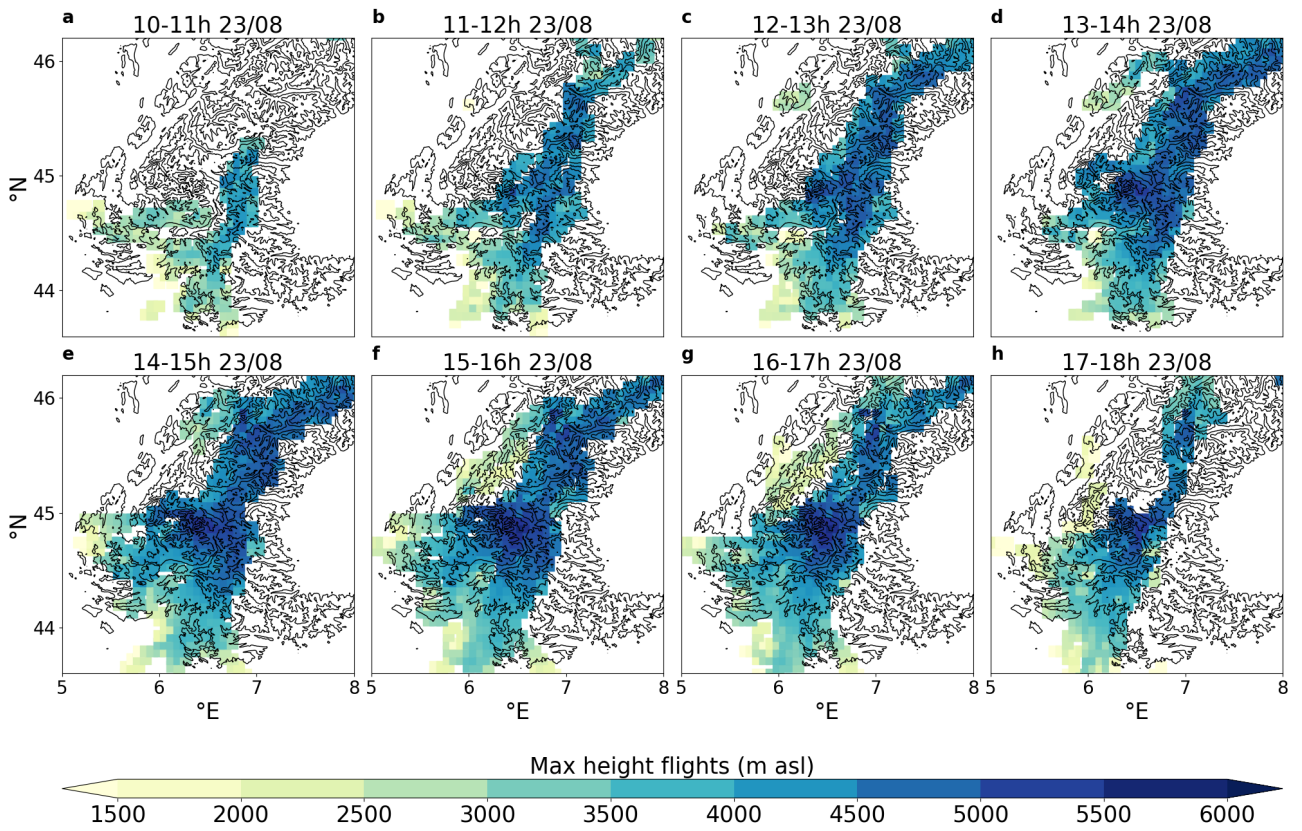


Figure 7 – Hourly maximum height reached by paragliding and gliding flights from 10 to 18h on a $10 \times 10 \text{ km}^2$ grid ($n = 50$ in section 3.3 on Sunday the 23th of August 2023. The background map shows 1000, 2000, 3000 iso-topography lines.

the number of flights covering the 10-11h time lapse is expected to be very low Fig.2, Fig.7(a) shall not be considered *legitimate*.

The ABL's daily cycle is shown on Fig.8. To each grid cell $10 \times 10 \text{ km}^2$ grid ($n = 50$, section 3.3) of the 19th of August is assigned an hourly variation of the maximum height reached. The eastern and western regions of the Alpine mountain range follow similar evolution though staggered over time. The eastern side is the first to ascend from 10 a.m. Fig.8(a) to 1 p.m. Fig.8(c). It is closely followed by the western side from 11 a.m. 8(b) to 2 p.m. 8(e). Similarly the eastern side is the first to subside from 2 p.m. Fig.8(d) to 7 p.m. Fig.8(h), closely followed by the western side from 3 p.m. Fig.8(e) to 7 p.m. Fig.8(h). The eastern/western staggered over time short wave radiative income may explains the similar, staggered over time evolution of the ABL (the southern Alpine mountain range being South-North oriented).

Fig.9(a) highlights the evolution of the observed maximum height reached distribution through time. Apart for the last two days, no qualitative difference is observed from the 19th to the 23th. The 23th shows a quite high maximum (6000 metres asl), which is consistent with that day having the highest cloud base of the six days. The 24th shows however a strong global depletion. This may be linked by the lack of flights available on the 24th, and the change in passageways due to upcoming storm, as discussed in section 3.2.1. Fig. 9(b) displays the evolution of the vertical wind distribution from the 19th to the 24th. The constant median of 4 m.s^{-1} from 10 a.m. until 2-4 p.m. describe a fully mixed and extended ABL with strong anabatic winds from mid-morning until mid-afternoon. This saturation might be linked to the ability of pilots (in median) to sample thermals currents more than to the atmosphere's dynamics. The decrease in the median vertical velocities from 2-4 p.m. until nighttime Fig. 9(b) displays the settlement of katabatic winds at late afternoon. This vertical

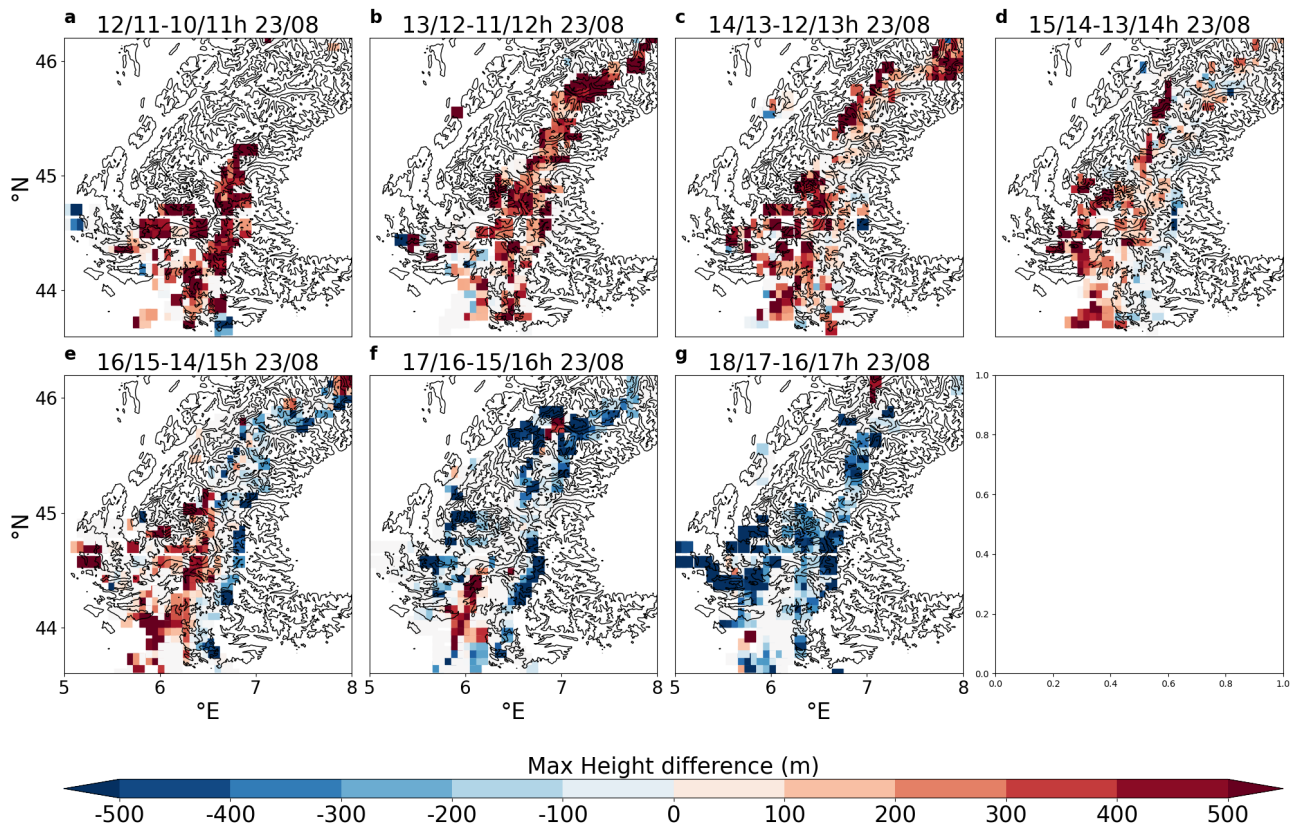


Figure 8 – Hourly variations of the maximum height reached by paragliding and gliding flights from 10 to 18h on a $10 \times 10 \text{ km}^2$ grid ($n = 50$ in section 3.3) on Sunday the 23th of August 2023. The background map shows 1000, 2000, 3000 iso-topography lines.

velocities depletion may explain to the global descent of the maximum height reached by flights from 2 p.m. until nighttime Fig. 9(a).

Horizontal and vertical wind components distribution highlights a strong spatial heterogeneity Fig.10 (a), in terms of intensity and direction. Fig.10(b) however shows that a coherent mesoscale wind direction and horizontal norm can be derived from the Fig.10(a) data on a coarser grid, which is consistent with a predominant elevated north-west wind in the Gap region that day (from a paragliding pilot's experience).

No investigation is further conducted on the 3D observed wind component. Indeed, the comparison of 3D rapidly varying, short small scale wind field with simulated snapshots might bring much complexity and uncertainties. Therefore, effort has yet been made to compare 3D values between observations and simulations.

4.2 Flights' comparison with models

In a first part are discussed the results from the comparison between the simulated and observed ABL's height (Fig. 11 12 13 (ad)). Then will be compared the observed and simulated vertical maximum speed values (Fig. 11 12 13 (eh)).

The spatial distributions Fig. 11 12 13(a) of observed values are quite similar to the simulated ones. The ABL's height scattered comparisons Fig. 11 12 13 (bc) firstly show the increase in ABL's height with the

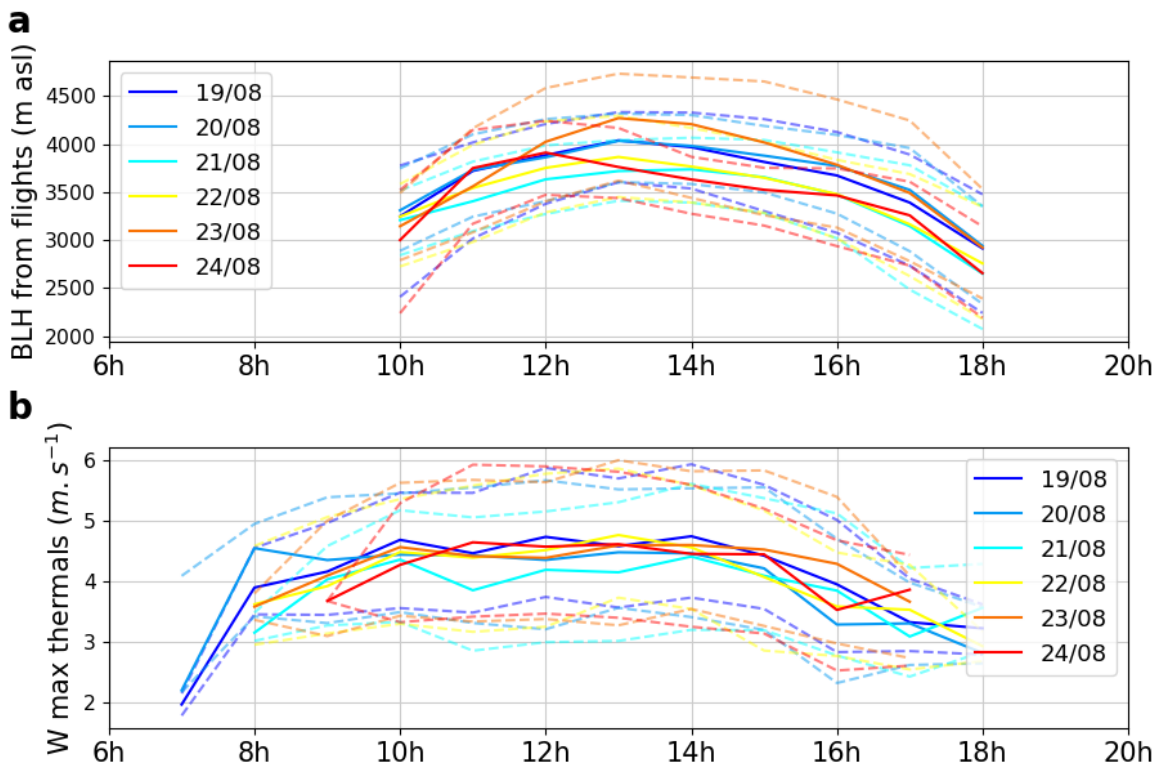


Figure 9 – Hourly maximum height reached during paragliding and gliding flights (a) within the $10 \times 10 \text{ km}^2$ grid ($n = 50$ in section 3.3) and (b) hourly maximum vertical speed inferred from thermalling flights for the six days from 19/08 to 24/08. Solid line correspond to the medians and the dashed lines to the lower and upper quartiles of the distributions.

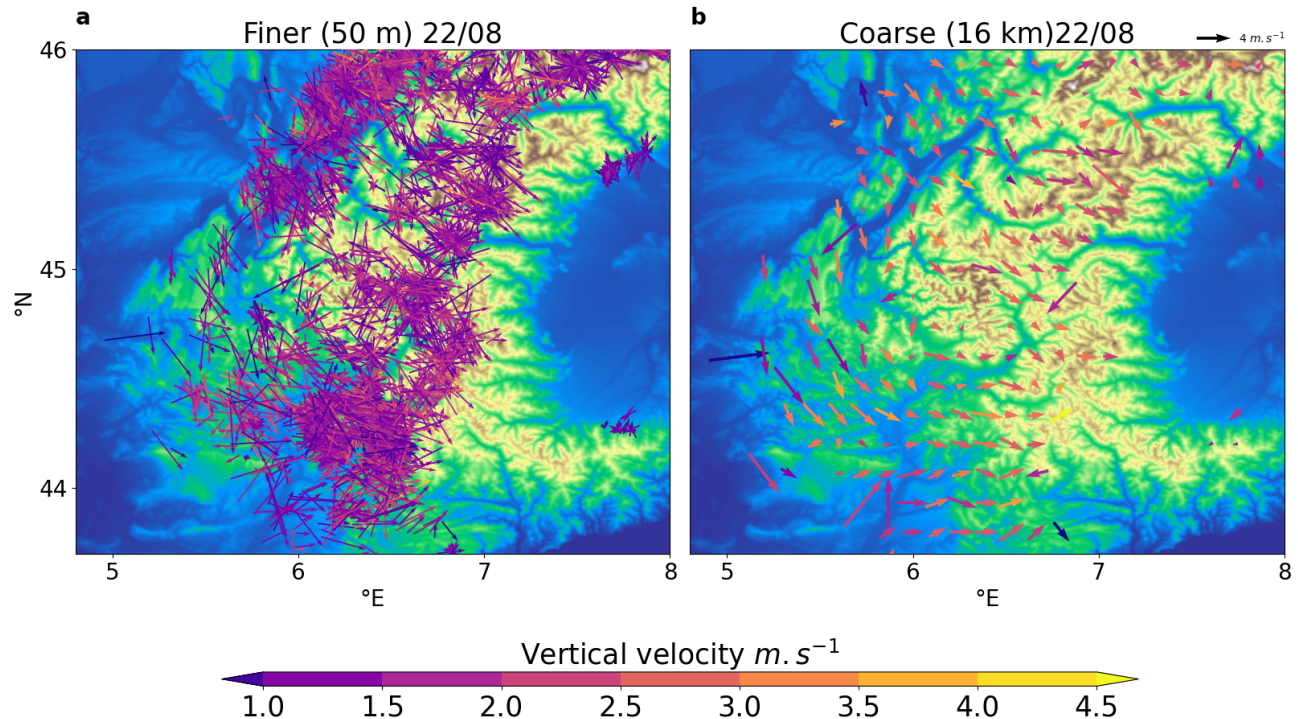


Figure 10 – ABL's horizontal and vertical wind inferred from paragliding and gliding data, as discuss in section 3.3, during Tuesday the 22th of August 2023, vertically projected on the surface. Colour, length and orientation of the arrows represent respectively the vertical speed, the horizontal speed and the horizontal direction. (b) is an interpolation of (a) on a regular grid of $16 \times 16 \text{ km}^2$ ($n = 25$ in 3.3) over the same domain. The background map shows the topography.

90^{th} quantile of the underlying altitude distribution. Regardless of the simulation, the concordance between observed and simulated values is better for high ABL's height values (also high 90^{th} quantile of the underlying altitude distribution). Moreover, regardless the underlying topography, the simulation overcomes the inferred value at 12 a.m. Fig. 11 12 13(b). This is reasonable considering that the observed maximum height provides information on the minimum ABL's height. Whatever the simulation, lower surface altitudes (under 2000 metres asl) highlight a high bias for the simulation values of at least 500 metres at 12 a.m. . Fig. 11 12 13(d) shows that this bias subsists until 2 p.m. . The situation inverses during the afternoon, reaching a negative bias from 5-6 p.m until 7 p.m. . In between takes place a maximal accordance of the simulated and observed distributions at 4-5 p.m. . However, one shall question the legitimacy of low underlying topography regions as theses regions are lesser *legitimate* 6. The *legitimacy* being it self time dependant. To better assess theses comparisons, a time dependant criteria of legitimacy shall be formulated. A final remark concerning the strong bias of the simulation relative to the observations at 3 p.m. Fig. 13(c) : Meso-NH 200 proposes a median boundary layer height of around 4000 metres asl, independent of the underlying topography, with a very narrow distribution. This may be partially explained by the strong ascending velocities Fig.13(g) described further, prompting an strongly mixed and vertically extended ABL. Indeed, the 12 a.m. scatter plot Fig.13(b), when simulated vertical velocities are less biased 13(f), does not show a topography independant ABL's height.

Fig. 11 12 13(e) display the vertical speed local accordance. The (nearly) total absence within the (simulated) observed values of negatives is expected at 12 a.m. with cloudless meteorological conditions in summer. The comparison between the ascending atmospheric currents within the three different simulations is discussed in the annexes A.2.

The Fig. 11 12 13(fg) scatter plot highlights that : AROME has a strong low bias and much narrow distribution, Meso-NH 600 shows a much better match in terms of interquantile extent and median, and Meso-NH 200 overestimate the observed median value with a similar interquantile extent. No influence of the thermalling ascents' elevations nor the flight's aircraft is demonstrated. Fig. 11 12 13(h) highlights this effect. As discussed in section 4.1, the flight's vertical maximum speed distribution's median saturate at 4 m.s^{-1} between 10 a.m. and 3 p.m. .This saturated period matches the *legitimate* high frequented period detailed in Fig. 2. Hence, the comparison between the observed and simulated values shall be more certain over this 10 a.m. to 4 p.m. period. The simulations show a much shorter saturation (2 to 3 p.m for AROME, 11 a.m. to 2 p.m. for Meso-NH 600 and 200) with different median values ($2-3 \text{ m.s}^{-1}$ for AROME, 4 and 6 m.s^{-1} for Meso-NH 600 and 200).

As AROME has a coarser resolution than Meso-NH, with parametrized shallow convection, the vertical mixing is mainly handled by its parametrization. As for Meso-NH, a finer resolution without shallow convection parametrization leads to a finer resolved shallow convection. Therefore, the difference in vertical speed sampling between the two models may arise from the effect of the parametrization of shallow convection. The more resolved simulation Meso-NH 200 admits a much stronger median saturation than the observed one. It is then tempting to suggest that the finer is the resolution the stronger will be the simulated vertical speeds. The vertical speeds shall however converge with the increase of the resolution.

Fig.13(h) Meso-NH 200 overcoming the observed vertical speeds is coherent with the ability of the flight's to provide a minimum of the maximum vertical speed values within the ABL. However, the early morning, lesser developed, ABL's observations offer nearly saturated vertical velocities (4 m.s^{-1} at 8H00) whereas the simulated vertical velocities distribution is much lesser whatever the simulation. The smaller size of the atmospheric vertical currents during morning, hence lesser resolved by Meso-NH, may explain the existence of observed strong vertical currents yet not resolved. This has to be put in perspective of the poor data quantity for

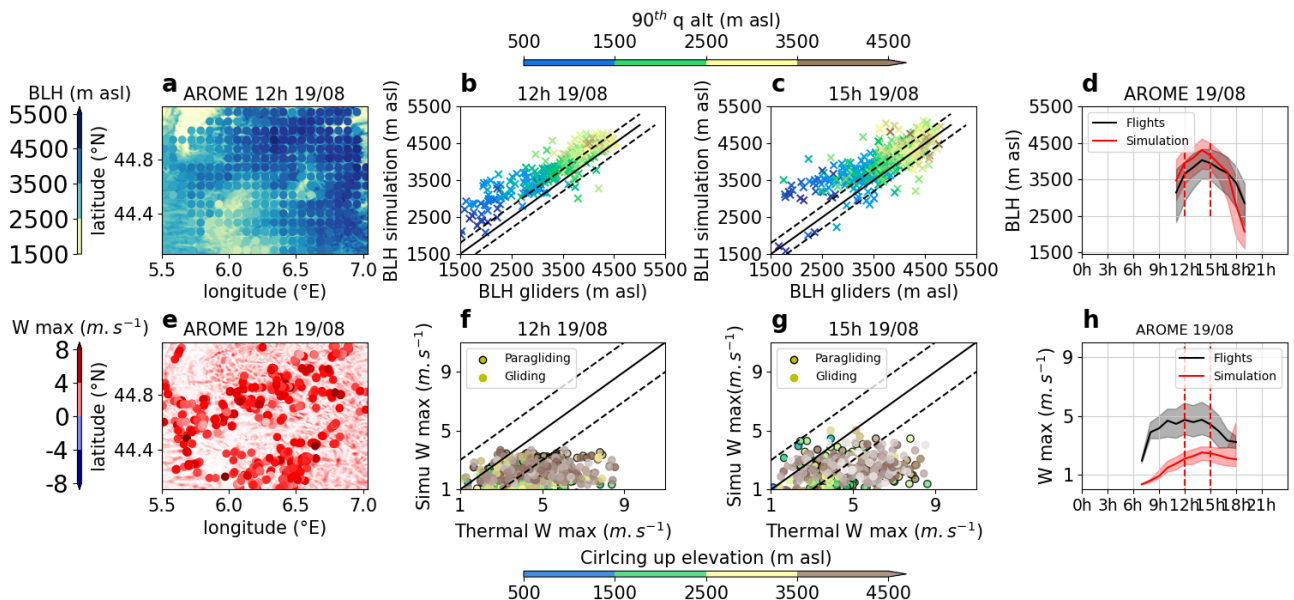


Figure 11 – ABL's height (abcd) and hourly maximum vertical velocities (efgh) the 19th of August on a 10 × 10 km² grid ($n = 50$), estimated from flight data and from AROME simulations at 1.3 km resolution: Spatial distribution (ae) of observations (dots) and model outputs (shading) and scatter plots simulation versus observation between 11H00 and 12H00 (bf) and 14H00 to 15H00 (cg). To each scattered dot is assigned a color referring to (b), (c) the 90th quantile of the underlying surface elevation distribution (within the corresponding 10 × 10 km² box of the mesh) and (f),(g) the mean elevation of the thermalling ascent from paragliding flights (black contour on the dots) and gliding flights (no black contour on the dots). The solid line represents the perfect accordance between inferred and simulated values. The dashed lines the overestimation (resp. underestimation) by the simulation of (b) and (c) 300 metres and (f) and (g) 1 m.s⁻¹ over the inferred values. Daily cycles are shown on (dh), with the median (solid line) and the interquartile range (shading).

early morning, with a little amount of flights.

The hours for the scatter plots are aiming at imaging two different atmospheric circulations. At 12 a.m., the slope winds are expected to be strongly settled and the valley breeze initiating. Whereas at 3 p.m., as the slope winds tend to decrease, the valley breeze shall be strongly settled.

4.3 Meteorological stations' comparison with models

The comparison between the models and the meteorological stations will be organise variable by variable, paragraph by paragraph, in the following order : θ , $\|U_h\|$ and R_v . For the sake of conciseness, only the comparison between observations and AROME 1.3 km will be discussed in this section. Analog comparisons with Meso-NH LES 600 and 200 are displayed within the annexes A.3.

As Fig.14(a) θ offers a quite good match, the scattered plot Fig.14(b) offers a more nuanced view. While the absolute difference between observed and stimulated values is lower than 4 °C for altitude higher than 2500 metres asl, the simulated lower altitude θ are much warmer at 5 a.m, regardless of the station's network. The 2 p.m. scatter plot Fig.14(c) offers an unbiased comparison, regardless of the station's altitude, nor the station's network. This low altitude warm bias is highlighted on Fig.14(d) where the simulated distribution of θ is constantly shifted of approximately +3 °C in regard to the observed distribution between 0 and 6 a.m. . The low altitude warm bias rapidly decrease until reaching a good match from 8 a.m. until 4 p.m. . The warm bias of surface θ during the night for all the models could be explained by an underestimated long wave radiative cooling or by a wrong representation of the turbulent mixing in the stable surface layer. Still, the simulated and

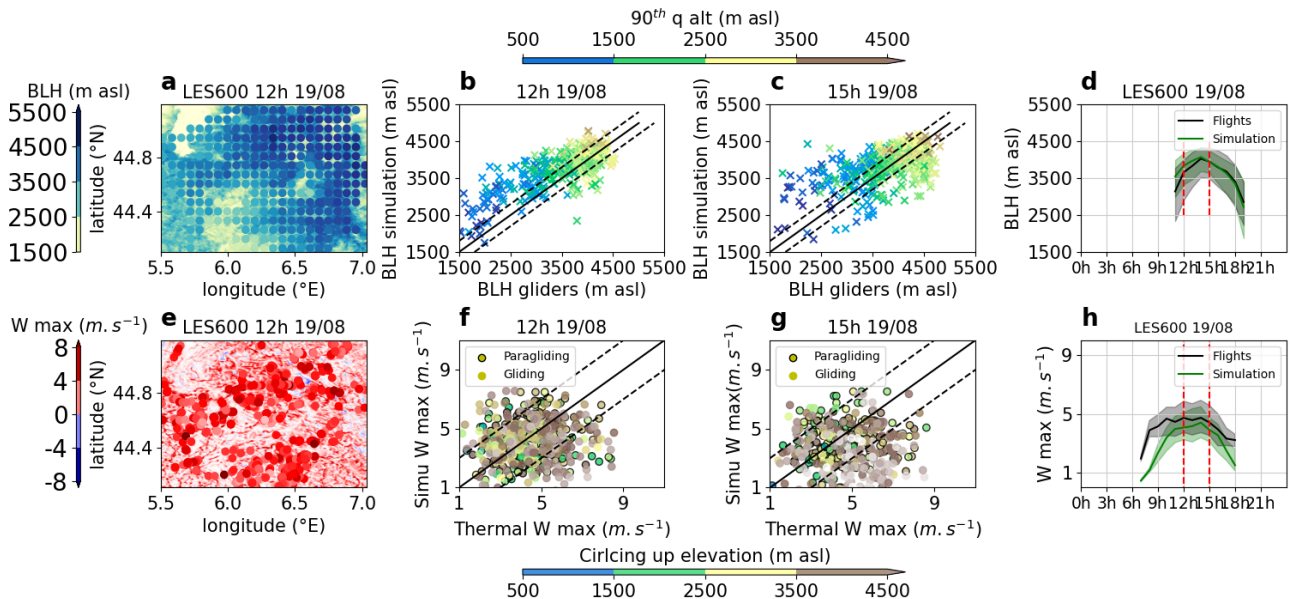


Figure 12 – Same as figure 11 for Meso-NH 600 metres.

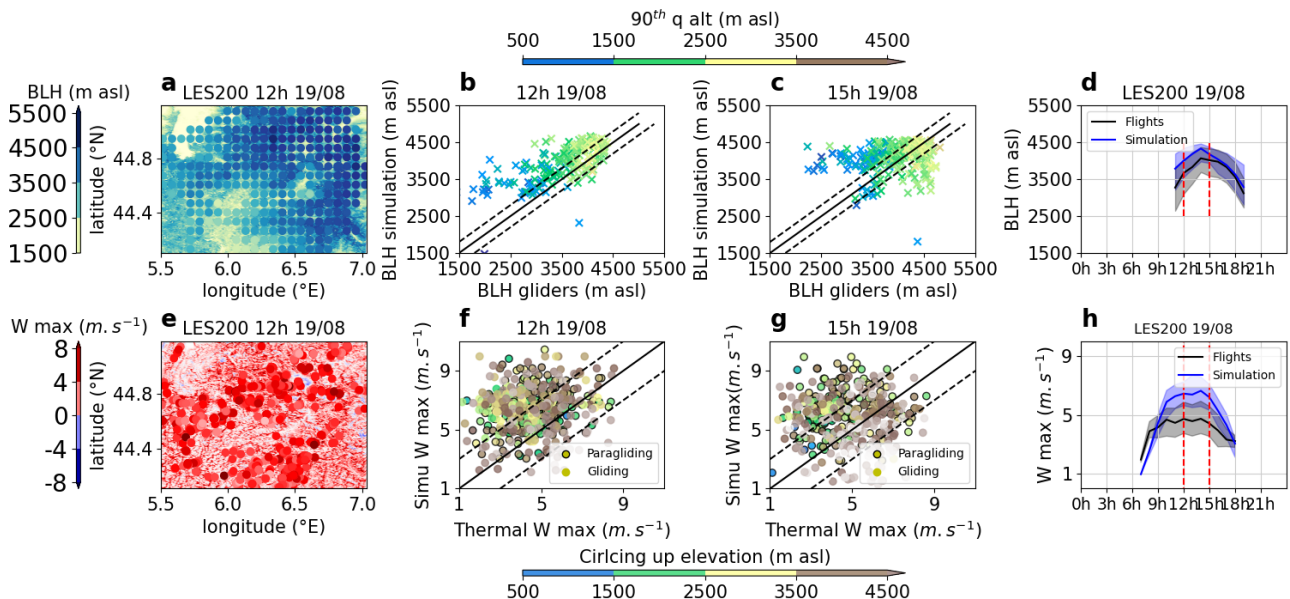


Figure 13 – Same as figure 11 for Meso-NH 200 metres.

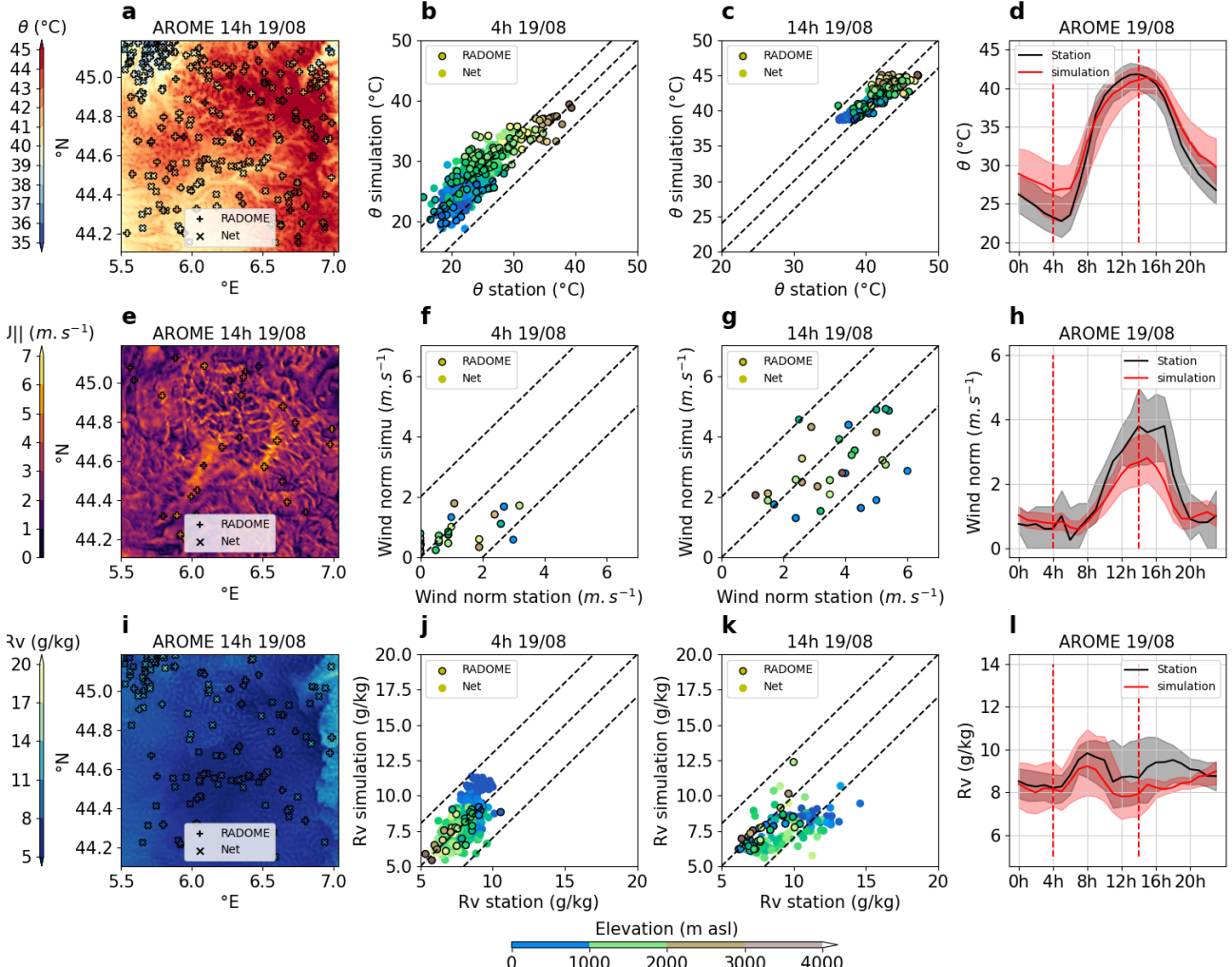


Figure 14 – Potential temperature θ (abcd), horizontal wind norm $||U_h||$ (efgh) and mixing ratio R_v (ijkl) the 19th of August, observed by stations and from AROME simulations at 1.3 km resolution : Spatial distribution (aeim) of observations (dots) and model outputs (shading) and scatter plots simulation versus observation at 4H00 (bfjn) and 14H00 (ciko). Each scattered dot is assigned a color referring to s Net (no black contour on the dots) or RADOME (black contour on the dots) station's elevation. The solid line represents the perfect accordance between inferred and simulated values. The dashed lines the overestimation (resp. underestimation) by the simulation of (bc) 4°C , (fg) $2 m.s^{-1}$, (jk) $3 g.kg^{-1}$ over the inferred values. Daily cycles are shown on (dhl), with the median (solid line) and the interquartile range (shading).

observed daily cycle's variations are quite similar. Lastly, Fig.14(bc) highlight the increase of θ with altitude on the surface in the observed and simulated values at 5 a.m. (the ABL is indeed stratified during nighttime) and 2 p.m. . The 2 p.m. ABL is however well mixed and not stratified. The altitude dependence of surface θ Fig.14(c) at 2 p.m. may be explained by (i) the mean increase of higher mountainous θ because of the "bulk" effect (section 2.1) resulting in valley wind, and (ii) θ at 2 metres elevation above ground is higher than the mean θ because it is impacted by the sensible flux. In the mountain, the surface layer slides up the slope, wind slope, warmed all the way up the summits. The surface θ is hence increased with elevation.

The norm of the horizontal wind $||U_h||$ comparison is not as accurate as the potential temperature θ . Please note that only the RADOME network is able to capture the wind norm. Firstly, Fig.14(e) highlights the short wavelengths variations of the simulated $||U_h||$ field, hence difficult to capture with the large scale RADOME network [Mandement and Caumont \[2020\]](#). For low synoptic forcing, the surface winds (valley and slope breeze) are much stronger during daytime than nighttime. As the largest valley breeze are resolved by AROME 1.3 km, the agreement is quite good with observations only during daytime Fig.14(eg). The unresolved small scale nighttime breeze is parametrized by AROME, hence not well fitted Fig.14(f). Lastly, the $||U_h||$ field's daily cycle's period is well fitted and its variations are well correlated with the simulation. However, a remarkable difference resides within the interquartile range Fig.14(h), though the variations of the interquartile range of the observed and simulated values appear to be correlated.

The water vapor mixing ratio R_v shows a nice fit Fig.14(ijkl). Firstly, while the RADOME network is fitted whatever the station's altitude, the Net network underline a strong time dependant bias on the lowest altitude stations Fig.14(jk). Within this domain, the lowest Net stations are mostly Grenoble's domestic stations. Indeed, M. Mandement's correction algorithm is base on comparisons between Net and RADOME stations [Mandement and Caumont \[2020\]](#). Two RADOME stations are available in the Grenoble area : one inside the city (close to the CEA), and one in the Chamrousse ski resort in altitude. As the correction algorithm for R_v is not accounting for altitude variations (θ algorithm does), the Net stations within Grenoble's area show biased water vapor mixing ratio values. This bias may correspond to a depletion of humidity around Chamrousse ski resort during nighttime caused by katabatic winds, and a increase of humidity around Chamrousse ski resort during daytime caused by the fusion of snow. This highlight the usefulness of Net stations and the necessity of improvement within mountainous areas. Secondly, the strongly stratified 4 a.m. snap shot Fig.14(j) highlights a elevation dependant R_v , higher surface atmosphere being dryer than lower surface atmosphere. Fig.14(ki) display a more mixed atmosphere, where the surface R_v is independent of the altitude. Lastly, the R_v field's daily cycle is well fitted and its variations are well correlated Fig.14(l). However, a remarkable difference resides within the interquartile range values, particularly strong from 11 a.m. to 8 p.m. .

It is crucial to remember that AROME assimilate the RADOME meteorological data 3.1.2. The AROME simulation comparison with RADOME stations Fig.14 strongly benefits from AROME's hourly assimilation of the RADOME data.

Fig.15 Resumes the temporal variations of the observed and simulated fields for the three simulations. One may remember from this plot the main remarks discussed above : Fig.15(a) As for the ABL, simulations tend to overcome the observed value until 5-6 p.m. when the situation inverses ; Fig.15(b) The ability to better sample the vertical maximum speed increases with the resolution of the simulation, only the Meso-NH 200 achieve to sample stronger vertical velocities than the flights. Even Meso-Nh 200 metres resolution fails to represent small scale early morning circulation ; Fig.15(c) All simulations have a low altitude warm bias during nighttime in potential temperature θ . While AROME reduces strongly this bias, Meso-NH 200 is closer to observation

than Meso-NH 600. AROME being more accurate than Meso-NH 600 and 200 is unexpected as the Meso-NH simulation is a downscaling from AROME. In fact, the downscaling process induced unexpected biases (too many clouds for instance) ; Fig.15(de) All simulations appear to fit the median variation's daily cycle and median values of the wind norm values $\|U_h\|$ and the water vapor mixing ratio R_v . Net correction algorithm needs to be improved to better fit mountainous areas.

5 Conclusion

A methodology has been developed to enhance RCMs' verification over complex terrain. Based on gliding and paragliding flights over the french Alps, the benefits from fine resolution and the use of flights were validated for rainless, no synoptic forcing conditions. This study underline several issues and results : **(i)** Gliding and paragliding flights are unique and valid data to efficiently cover a large spatial and temporal extent within the ABL. **(ii)** AROME show high skill for meteorological variables, whereas Meso-NH is a performing tool to simulate vertical velocities **(iii)** A higher resolution provides a better accuracy for a given atmospheric RCMs, though AROME 1.3 km proved better than Meso-NH 600 m and 200 m from meteorological variables. Overall, this study highlights the necessity to incorporate new data of atmospheric dynamics within the ABL, such as paragliding and gliding flights, to allow a full evaluation and tuning of RCMs, in particular over mountainous areas.

Paragliding and gliding flights have still some more tricks up their sleeve. Further research may be done with the use of gliding and paragliding, considering cloud's pictures, reconstructing 3D wind fields from flights, considering the assimilation of controlled daily paragliding flights over specific regions.

References

- Sultan Al-Yahyai, Yassine Charabi, and Adel Gastli. Review of the use of numerical weather prediction (nwp) models for wind energy assessment. *Renewable and Sustainable Energy Reviews*, 14(9):3192–3198, 2010.
- Akio Arakawa. The cumulus parameterization problem: Past, present, and future. *Journal of climate*, 17(13):2493–2525, 2004.
- Michael Baldauf, Axel Seifert, Jochen Förstner, Detlev Majewski, Matthias Raschendorfer, and Thorsten Reinhardt. Operational convective-scale numerical weather prediction with the cosmo model: Description and sensitivities. *Monthly Weather Review*, 139(12):3887–3905, 2011.
- I. Bashmachnikov, C.M. Loureiro, and A. Martins. Topographically induced circulation patterns and mixing over condor seamount. *Deep Sea Research Part II: Topical Studies in Oceanography*, 98:38–51, 2013. ISSN 0967-0645. doi:<https://doi.org/10.1016/j.dsr2.2013.09.014>. URL <https://www.sciencedirect.com/science/article/pii/S0967064513003457>. An Integrated Approach for Studying Seamounts: CONDOR Observatory.
- Peter Bauer, Alan Thorpe, and Gilbert Brunet. The quiet revolution of numerical weather prediction. *Nature*, 525(7567):47–55, 2015.
- Diego Muniz Benedetti. Paragliders flight dynamics. *Universidade Federal de Minas Gerais*, 2012. URL <http://hdl.handle.net/1843/BUOS-95RGS5>.

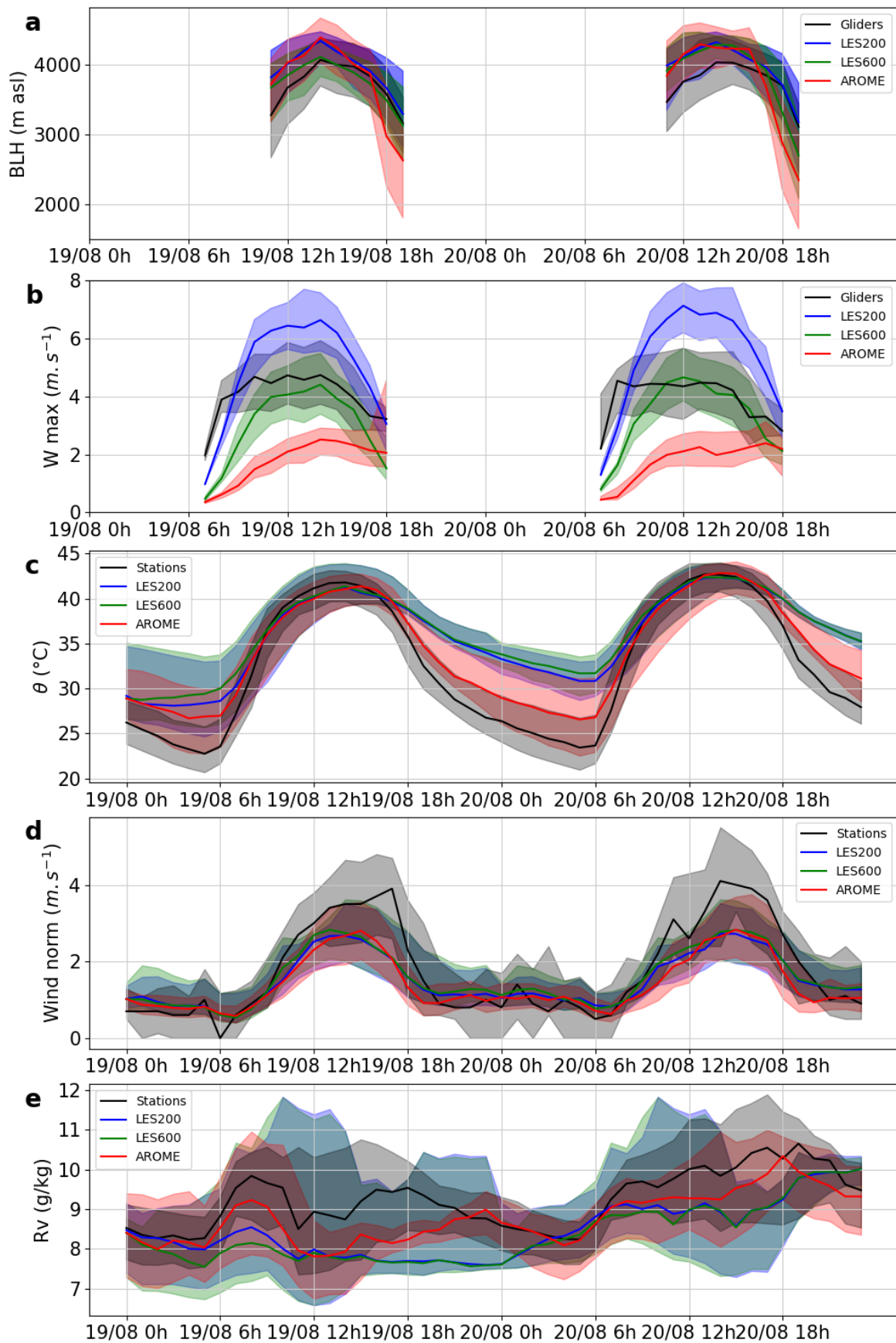


Figure 15 – Daily cycle of **(a)** ABL's height (m asl), **(b)** maximum vertical speed ($m.s^{-1}$), **(c)** potential temperature θ ($^{\circ}C$), **(d)** horizontal wind norm $||U_h||$ ($m.s^{-1}$) and **(e)** water vapor mixing ratio R_v ($g.kg^{-1}$) for observations (black line), Meso-NH LES 600 (green line), Meso-NH LES 200 (blue line) and AROME (red line) the 19th and 20th. The shading represent the interquartile range.

Alexander Blass, Xiaojue Zhu, Roberto Verzicco, Detlef Lohse, and Richard J. A. M. Stevens. Flow organization and heat transfer in turbulent wall sheared thermal convection. *Journal of Fluid Mechanics*, 897:A22, 2020. doi:10.1017/jfm.2020.378.

P. Bougeault, A. Jansa Clar, B. Benech, B. Carissimo, J. Pelon, and E. Richard. Momentum budget over the pyrénées: The pyrex experiment. *Bulletin of the American Meteorological Society*, 71(6):806 – 818, 1990. doi:10.1175/1520-0477(1990)071<0806:MBOTPT>2.0.CO;2. URL https://journals.ametsoc.org/view/journals/bams/71/6/1520-0477_1990_071_0806_mbotpt_2_0_co_2.xml.

Philippe Bougeault and Pierre Lacarrere. Parameterization of orography-induced turbulence in a mesobeta-scale model. *Monthly weather review*, 117(8):1872–1890, 1989.

Philippe Bougeault, Peter Binder, A. Buzzi, R. Dirks, R. Houze, J. Kuettner, Ronald Smith, Reinhold Steinacker, and Hans Volkert. The map special observing period. *Bulletin of the American Meteorological Society*, 82: 433–462, 03 2001. doi:10.1175/1520-0477(2001)082<0433:TMSOP>2.3.CO;2.

Fotini Katopodes Chow, Christoph Schär, Nikolina Ban, Katherine A. Lundquist, Linda Schlemmer, and Xiaoming Shi. Crossing multiple gray zones in the transition from mesoscale to microscale simulation over complex terrain. *Atmosphere*, 10(5), 2019. ISSN 2073-4433. doi:10.3390/atmos10050274. URL <https://www.mdpi.com/2073-4433/10/5/274>.

PHILIPPE Courtier, J-N Thépaut, and Anthony Hollingsworth. A strategy for operational implementation of 4d-var, using an incremental approach. *Quarterly Journal of the Royal Meteorological Society*, 120(519): 1367–1387, 1994.

Bo Criss. History of paragliding. URL <https://web.archive.org/web/20090913071154/http://www.circlinghawk.com/history.html>.

J. Cuxart, B. Wrenger, D. Martínez-Villagrassa, J. Reuder, M. O. Jonassen, M. A. Jiménez, M. Lothon, F. Lohou, O. Hartogensis, J. Dünnemann, L. Conangla, and A. Garai. Estimation of the advection effects induced by surface heterogeneities in the surface energy budget. *Atmospheric Chemistry and Physics*, 16(14):9489–9504, 2016. doi:10.5194/acp-16-9489-2016. URL <https://acp.copernicus.org/articles/16/9489/2016/>.

Joan Cuxart. When can a high-resolution simulation over complex terrain be called les? *Frontiers in Earth Science*, 3, 2015. ISSN 2296-6463. doi:10.3389/feart.2015.00087. URL <https://www.frontiersin.org/articles/10.3389/feart.2015.00087>.

H.C. Davies and H. Pichler. *Mountain Meteorology and ALPEX*. Meteorology and atmospheric physics. Springer-Verlag, 1990. URL <https://books.google.fr/books?id=PiwozWEACAAJ>.

Fla. D.C. Jalbert, B. Raton. Multi-cell wing type aerial device. URL <https://patentimages.storage.googleapis.com/09/c6/f3/314eda8c5a5117/US3285546.pdf>.

Gert-Jan Duine and Stephan FJ De Wekker. The effects of horizontal grid spacing on simulated daytime boundary layer depths in an area of complex terrain in utah. *Environmental Fluid Mechanics*, 20:1313–1331, 2020.

Claude Fischer, Thibaut Montmerle, Loïk Berre, Ludovic Auger, and Simona Ecaterina ȘTEFĂNESCU. An overview of the variational assimilation in the aladin/france numerical weather-prediction system. *Quarterly Journal of the Royal Meteorological Society*, 131(613):3477–3492, 2005.

doi:<https://doi.org/10.1256/qj.05.115>. URL <https://rmets.onlinelibrary.wiley.com/doi/abs/10.1256/qj.05.115>.

Météo France. Arome. *Météo France*, 2008. URL <https://www.umr-cnrm.fr/spip.php?article120>.

R. Hierro, H. Pessano, P. Llamedo, A. de la Torre, P. Alexander, and A. Odiard. Orographic effects related to deep convection events over the andes region. *Atmospheric Research*, 120-121:216–225, 2013. ISSN 0169-8095. doi:<https://doi.org/10.1016/j.atmosres.2012.08.020>. URL <https://www.sciencedirect.com/science/article/pii/S0169809512002876>.

Rachel Honnert, Fleur Couvreux, Valéry Masson, and Dávid Lancz. Sampling the structure of convective turbulence and implications for grey-zone parametrizations. *Boundary-layer meteorology*, 160:133–156, 2016.

Jackie. Glider_{max}. URL.

N. Kalthoff, H.-J. Binder, M. Kossmann, R. VÖgtlin, U. Corsmeier, F. Fiedler, and H. Schlager. Temporal evolution and spatial variation of the boundary layer over complex terrain. *Atmospheric Environment*, 32(7):1179–1194, 1998. ISSN 1352-2310. doi:[https://doi.org/10.1016/S1352-2310\(97\)00193-3](https://doi.org/10.1016/S1352-2310(97)00193-3). URL <https://www.sciencedirect.com/science/article/pii/S1352231097001933>.

Daniel J Kirshbaum, Bianca Adler, Norbert Kalthoff, Christian Barthlott, and Stefano Serafin. Moist orographic convection: Physical mechanisms and links to surface-exchange processes. *Atmosphere*, 9(3):80, 2018.

C. Lac, J.-P. Chaboureau, V. Masson, J.-P. Pinty, P. Tulet, J. Escobar, M. Leriche, C. Barthe, B. Aouizerats, C. Augros, P. Aumond, F. Auguste, P. Bechtold, S. Berthet, S. Bielli, F. Bosseur, O. Caumont, J.-M. Cohard, J. Colin, F. Couvreux, J. Cuxart, G. Delautier, T. Dauhut, V. Ducrocq, J.-B. Filippi, D. Gazen, O. Geoffroy, F. Gheusi, R. Honnert, J.-P. Lafore, C. Lebeaupin Brossier, Q. Libois, T. Lunet, C. Mari, T. Maric, P. Mascart, M. Mogé, G. Molinié, O. Nuissier, F. Pantillon, P. Peyrillé, J. Pergaud, E. Perraud, J. Pianezze, J.-L. Redelsperger, D. Ricard, E. Richard, S. Riette, Q. Rodier, R. Schoetter, L. Seyfried, J. Stein, K. Suhre, M. Taufour, O. Thouron, S. Turner, A. Verrelle, B. Vié, F. Visentin, V. Vionnet, and P. Wautelet. Overview of the meso-nh model version 5.4 and its applications. *Geoscientific Model Development*, 11(5):1929–1969, 2018. doi:[10.5194/gmd-11-1929-2018](https://doi.org/10.5194/gmd-11-1929-2018). URL <https://gmd.copernicus.org/articles/11/1929/2018/>.

Stein J. Asencio N. Bougeault P. Ducrocq V. Duron J. AU Fischer C. Héreil P. Mascart P. Masson V. Pinty J. P. Redelsperger J. L. Richard E. de Arellano J. Vilà-Guerau Lafore, J. P. The meso-nh atmospheric simulation system. part i: adiabatic formulation and control simulations. 1997. doi:[10.1007/s00585-997-0090-6](https://doi.org/10.1007/s00585-997-0090-6). URL <https://doi.org/10.1007/s00585-997-0090-6>.

L. Laiti, D. Zardi, M. de Franceschi, G. Rampanelli, and L. Giovannini. Analysis of the diurnal development of a lake-valley circulation in the alps based on airborne and surface measurements. *Atmospheric Chemistry and Physics*, 14(18):9771–9786, 2014. doi:[10.5194/acp-14-9771-2014](https://doi.org/10.5194/acp-14-9771-2014). URL <https://acp.copernicus.org/articles/14/9771/2014/>.

Nicholas Landell-Mills. Paragliding explained by newtonian physics., 07 2021.

Margaret A. LeMone and William T. Pennell. The relationship of trade wind cumulus distribution to sub-cloud layer fluxes and structure. *Monthly Weather Review*, 104(5):524 – 539, 1976. doi:[10.1175/1520-](https://doi.org/10.1175/1520-)

0493(1976)104<0524:TROTWC>2.0.CO;2. URL https://journals.ametsoc.org/view/journals/mwre/104/5/1520-0493_1976_104_0524_trotwc_2_0_co_2.xml.

Edward N Lorenz. Energy and numerical weather prediction. *Tellus*, 12(4):364–373, 1960.

M. Lothon, F. Lohou, D. Pino, F. Couvreux, E. R. Pardyjak, J. Reuder, J. Vilà-Guerau de Arellano, P. Durand, O. Hartogensis, D. Legain, P. Augustin, B. Gioli, D. H. Lenschow, I. Faloona, C. Yagüe, D. C. Alexander, W. M. Angevine, E. Bargain, J. Barrié, E. Bazile, Y. Bezombes, E. Blay-Carreras, A. van de Boer, J. L. Boichard, A. Bourdon, A. Butet, B. Campistron, O. de Coster, J. Cuxart, A. Dabas, C. Darbieu, K. Deboudt, H. Delbarre, S. Derrien, P. Flament, M. Fourmentin, A. Garai, F. Gibert, A. Graf, J. Groebner, F. Guichard, M. A. Jiménez, M. Jonassen, A. van den Kroonenberg, V. Magliulo, S. Martin, D. Martinez, L. Mastrorillo, A. F. Moene, F. Molinos, E. Moulin, H. P. Pietersen, B. Piguet, E. Pique, C. Román-Cascón, C. Rufin-Soler, F. Saïd, M. Sastre-Marugán, Y. Seity, G. J. Steeneveld, P. Toscano, O. Traullé, D. Tzanos, S. Wacker, N. Wildmann, and A. Zaldei. The bllast field experiment: Boundary-layer late afternoon and sunset turbulence. *Atmospheric Chemistry and Physics*, 14(20):10931–10960, 2014. doi:10.5194/acp-14-10931-2014. URL <https://acp.copernicus.org/articles/14/10931/2014/>.

DV Mahalakshmi, KVS Badarinath, and CV Naidu. Influence of boundary layer dynamics on pollutant concentrations over urban region—a study using ground based measurements. *92.60. Mt; 92.60. Sz*, 2011.

Marc Mandement and Olivier Caumont. Contribution of personal weather stations to the observation of deep-convection features near the ground. *Natural Hazards and Earth System Sciences*, 20(1):299–322, 2020.

Luiz E. Medeiros and David R. Fitzjarrald. Stable boundary layer in complex terrain. part ii: Geometrical and sheltering effects on mixing. *Journal of Applied Meteorology and Climatology*, 54(1):170 – 188, 2015. doi:10.1175/JAMC-D-13-0346.1. URL <https://journals.ametsoc.org/view/journals/apme/54/1/jamc-d-13-0346.1.xml>.

Hugh Miller. How fast is it? how we test paraglider speeds. URL <https://xcmag.com/magazine-articles/how-fast-does-it-go-testing-paraglider-speeds/>.

Diego Monteiro, Cécile Caillaud, Raphaëlle Samacoïts, Matthieu Lafaysse, and Samuel Morin. Potential and limitations of convection-permitting cnrm-arome climate modelling in the french alps. *International Journal of Climatology*, 42(14):7162–7185, 2022.

Schoetter Robert Masson Valéry Lac Christine Carissimo Bertrand Nagel, Tim. Numerical analysis of the atmospheric boundary-layer turbulence influence on microscale transport of pollutant in an idealized urban environment. *Boundary-Layer Meteorology*, 2022. doi:10.1007/s10546-022-00697-7. URL <https://doi.org/10.1007/s10546-022-00697-7>.

Julien Pergaud, Valéry Masson, Sylvie Malardel, and Fleur Couvreux. A parameterization of dry thermals and shallow cumuli for mesoscale numerical weather prediction. *Boundary-layer meteorology*, 132:83–106, 2009.

Fred Pieri. Ozone sharknose technology. URL <https://flyozone.com/paragliders/infozone/ozone-sharknose-technology>.

Oliver Reitebuch, Alain Dabas, Patricia Delville, Philippe Drobinski, and Leonhard Gantner. Characterisation of „alpine pumping“ by airborne doppler lidar and numerical simulations. In *Int. Conf. Alp. Meteor., Brig*, pages 134–137, 2003.

Catherine Rio and Frédéric Hourdin. Understand and simulate scale interactions. 2023.

Mina Rohanizadegan, Richard M. Petrone, John W. Pomeroy, Branko Kosovic, Domingo Muñoz-Esparza, and Warren D. Helgason. High-resolution large-eddy simulations of flow in the complex terrain of the canadian rockies. *Earth and Space Science*, 10(10):e2023EA003166, 2023. doi:<https://doi.org/10.1029/2023EA003166>. URL <https://agupubs.onlinelibrary.wiley.com/doi/abs/10.1029/2023EA003166>. e2023EA003166 2023EA003166.

Mathias W Rotach and Dino Zardi. On the boundary-layer structure over highly complex terrain: Key findings from map. *Quarterly Journal of the Royal Meteorological Society: A journal of the atmospheric sciences, applied meteorology and physical oceanography*, 133(625):937–948, 2007.

Mathias W. Rotach, Alexander Gohm, Moritz N. Lang, Daniel Leukauf, Ivana Stiperski, and Johannes S. Wagner. On the vertical exchange of heat, mass, and momentum over complex, mountainous terrain. *Frontiers in Earth Science*, 3, 2015. ISSN 2296-6463. doi:[10.3389/feart.2015.00076](https://doi.org/10.3389/feart.2015.00076). URL <https://www.frontiersin.org/articles/10.3389/feart.2015.00076>.

R. Soleil. Accidentologie du parapente chez les compétiteurs. URL <https://dumas.ccsd.cnrs.fr/dumas-01338714/document>.

Roland B. Stull. *An Introduction to Boundary Layer Meteorology*. Springer Dordrecht, 1998. doi:<https://doi.org/10.1007/978-94-009-3027-8>.

Jean Tardieu and Michel Leroy. Radome, le réseau temps réel d’observation au sol de météo-france. *La Météorologie*, 2003(40):40–43, 2003.

Piet Termonia, Claude Fischer, Eric Bazile, François Bouyssel, Radvila Brozkova, Pierre Bénard, Bogdan Bochenek, Daan Degrauwe, Mária Derková, Ryad Khatib, Rafiq Hamdi, Ján Mašek, Patricia Pottier, Neva Pristov, Yann Seity, Petra Smolikova, Oldřich Španiel, Martina Tudor, Yong Wang, and Alain Joly. The aladin system and its canonical model configurations arome cy41t1 and alaro cy40t1. *Geoscientific Model Development*, 11:257–281, 01 2018. doi:[10.5194/gmd-11-257-2018](https://doi.org/10.5194/gmd-11-257-2018).

Textile. The envelope. URL <http://www.eballoon.org/balloon/envelope.html>.

Steve Uzochukwu. Paragliding lines. URL <https://web.archive.org/web/20111029221547/http://www.ojovolador.com/eng/read/reports/lines/index.html>.

Simon Vosper, Emilie Carter, Humphrey Lean, Adrian Lock, Peter Clark, and Stuart Webster. High resolution modelling of valley cold pools. *Atmospheric Science Letters*, 14(3):193–199, 2013. doi:<https://doi.org/10.1002/asl2.439>. URL <https://rmets.onlinelibrary.wiley.com/doi/abs/10.1002/asl2.439>.

Johannes S. Wagner, Alexander Gohm, and Mathias W. Rotach. The impact of horizontal model grid resolution on the boundary layer structure over an idealized valley. *Monthly Weather Review*, 142(9):3446 – 3465, 2014.

doi:10.1175/MWR-D-14-00002.1. URL <https://journals.ametsoc.org/view/journals/mwre/142/9/mwr-d-14-00002.1.xml>.

Nils P Wedi, Karim Yessad, and Agathe Untch. *The nonhydrostatic global IFS/ARPEGE: model formulation and testing*. ECMWF Reading, UK, 2009.

Wikipedia. Gliding, a. URL <https://en.wikipedia.org/wiki/Gliding>.

Wikipedia. Paragliding, b. URL https://en.wikipedia.org/wiki/Paragliding#cite_note-13.

Bowen Zhou, Jason S Simon, and Fotini K Chow. The convective boundary layer in the terra incognita. *Journal of the Atmospheric Sciences*, 71(7):2545–2563, 2014.

Acknowledgements

I would like to say a big thank to my two supervisors who taught me a lot, with a lot of patience and beautiful maps. Special thanks to Catherine Rio, Fleur Couvreux and Marc Mandement for their input, suggestions and remarks. Even more special thanks to Zoé Derré, famous cartographer, for her precious cartographic advices.

A Annexes

A.1 Thermal elevation's distribution

Fig.16 offers another view of the usefulness of paragliding and gliding flights data to infer ABL's characteristics. Firstly, the hourly number of thermalling ascents highlights the lapse time of *legitimacy*, from 9H00 to 17H00. Then, the variations and maximum of the elevation of the hourly maximum number of thermalling ascents highlight the ABL's daily cycle : a growth from early morning until 14H00, herein shown by a high number of thermalling ascents covering a vast elevation range (well mixed ABL) until high maximum elevation (ABL's height). Followed by a decreasing number of thermalling ascents (decreasing of slope winds) though still covering a large elevation range (well mixed ABL) until still high but slightly decreasing maximal elevation (ABL's height) from 14H00 to 16H00. And finally a strong decreasing number of thermalling ascents (strong weakening of anabatic winds) covering a narrow elevation range (ABL in the early process of stratification) until decreasing maximal elevation (ABL's height) from 17H00 until next morning. This analysis could be improved by better quantifying the uses and customs of pilots, which surely impact the figure 16.

A.2 Convection sampling

The convection organisation in AROME 1.3 km, Meso-NH LES 600 m and Meso-NH LES 200 metres are compared in Fig.17. The three simulations show much different convection's organisation on the same domain at the same hour, only twelve hours after shared initialisation. Firstly, AROME shows a lack of contrast with much lower maximal vertical velocities than Meso-NH LES 600 and 200 (Fig.15 as well). As the low scale topography following convection is not captured by AROME 1.3 km, Meso-NH LES 600 and 200 display a much more detailed, terrain following convection. The same observation takes place between Meso-NH LES 600 and 200 simulations. Moreover, the LES 200 convection is then organised into plumes rather than LES 600 rolls. Hence Meso-NH LES 200 is in better accordance with the state of the art representation of high Reynolds number buoyantly forced convection [Blass et al., 2020]. It is therefore tempting to propose that better sampling

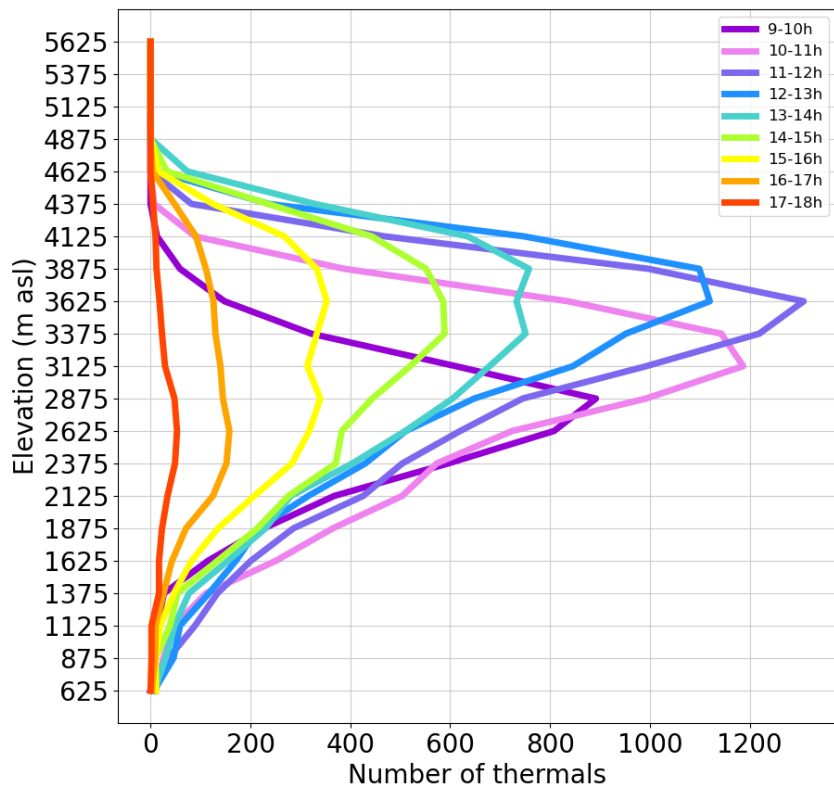


Figure 16 – Hourly number of thermals (defined with the 5's method) as a function of elevation asl on Sunday the 19th of August.

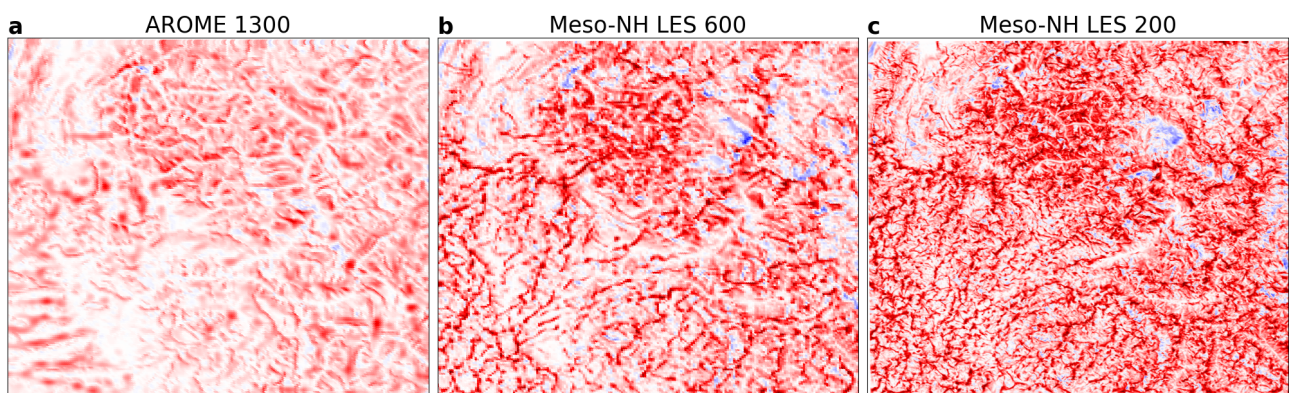


Figure 17 – Maximum vertical velocity of (a) AROME 1300 m (b) Meso-NH LES 600 m and (c) Meso-NH LES 200 m at 12H00 on Sunday the 19th of August.

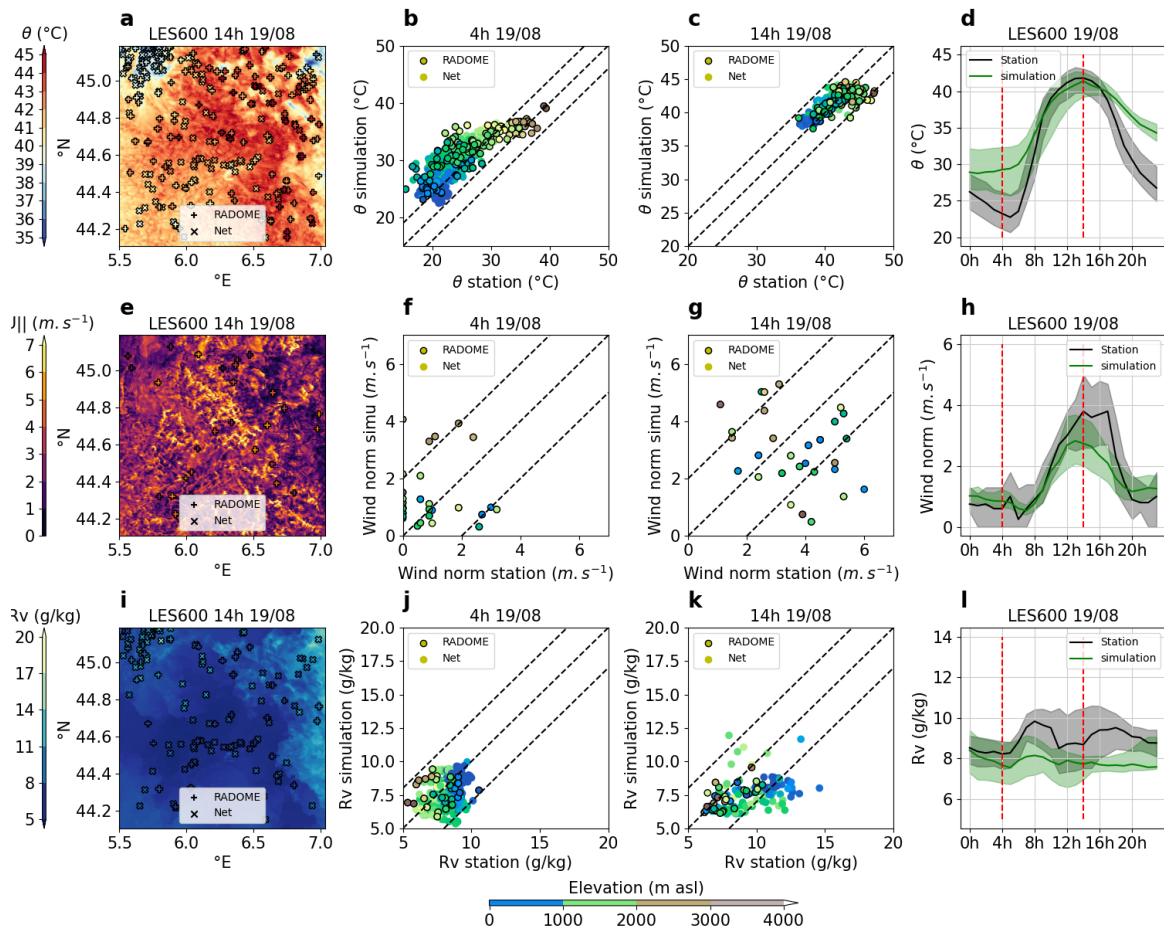


Figure 18 – Idem as figure 14 for Meso-NH 600 metres.

of the topography is key to enhance ABL's simulation accuracy to reproduce convection over complex terrain [Wagner et al., 2014].

A.3 Surface variables for Meso-NH 600 and 200 m

The observations discussed in section 4.3 are valid for Meso-NH 600 (Fig.18) and 200 (Fig.19). The low altitude warm bias in potential temperature θ during nighttime is stronger for Meso-NH 600 than 200, though greater than AROME's. Meso-NH 200 simulates better the water vapor mixing ratio R_v and horizontal wind norm $||U_h||$ than Meso-NH 600, thought lesser well than AROME. It is crucial to keep in mind that Meso-NH does not assimilate the RADOME meteorological data hourly like AROME. Therefore, the lesser accordance between Meso-NH and observed θ , R_v and $||U_h||$ was expected.

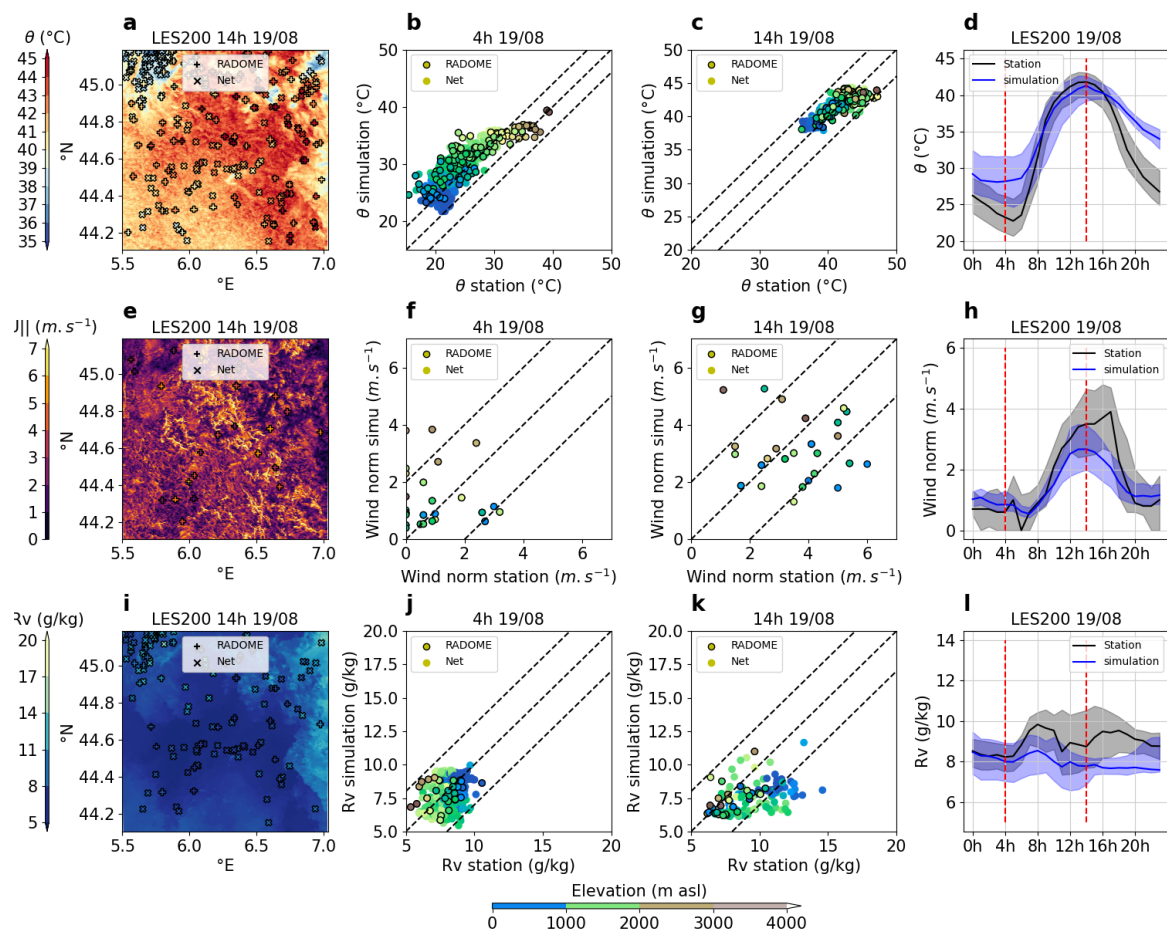


Figure 19 – Idem as figure 14 for Meso-NH 200 metres.

